

Thesis Title

A subtitle of your thesis

Author name



Thesis submitted for the degree of
Master in Master's Program Name <change at
main.tex>
60 credits

Department Name <change at main.tex>
Faculty name <change in duoforside.tex>

UNIVERSITY OF OSLO

Spring 2022

Thesis Title

A subtitle of your thesis

Author name

© 2022 Author name

Thesis Title

<http://www.duo.uio.no/>

Printed: Reprosentralen, University of Oslo

Abstract

Contents

1	Introduction	1
I Theory		3
2	High-Entropy alloys	4
2.1	Fundamentals	4
2.2	Core effects and properties	7
3	Modeling of random alloys	9
3.1	The Special Quasi-random Structure model	9
3.1.1	Mathematical description	10
3.1.2	Applications to high-entropy alloys	12
4	Density Functional Theory	16
4.1	Review of Quantum Mechanics	17
4.1.1	The Shrödinger equation	17
4.1.2	Approximations to the many-body Shrödinger equation	18
4.2	Kohn-Sham density functional theory	20
4.2.1	Density functional theory	20
4.2.2	The Kohn-Sham Equation	21
4.3	Limitations of DFT	22
II Method		24
5	Practical aspects of DFT	25
5.1	The Exchange-Correlation functional	25
5.1.1	Local density approximation	25
5.1.2	Generalized gradient approximation	26
5.1.3	Meta-GGA	26
5.1.4	Hybrid functionals	27
5.1.5	Outlook	27
5.2	Plane waves and reciprocal space	28
5.3	Self-consistent field calculation	30

6 Computational details	32
6.1 Settings and dependencies	32
6.2 Material	33
III Results and Discussion	35
7 The high-entropy silicide (CrFeMnNi)Si₂	36
7.1 Bulk β - FeSi ₂	36
7.2 (CrFeMnNi)Si ₂ SQSs	37
7.2.1 The band gap	39
7.2.2 Local and projected density of states	43
7.2.3 The band gap with SCAN and HSE06	45
7.2.4 Pair distribution functions	50
7.2.5 Charge density	51
7.2.6 SQS size	52
8 Alternative compositions	56
8.1 Exploring the quaternary phase diagram	56
8.2 High entropy silicides with cobalt/titanium	60
IV Conclusion	66
A Cr₄Fe₄Mn₄Ni₄Si₃₂	68
A.1 Density of states	68
A.2 Projected density of states	70
A.3 Charge density	71
B Alternative compositions	72

List of Figures

2.1	Formation of HEA based on δ and N . Figures adopted from [heav2016_ch2]	6
2.2	A schematic illustration of lattice distortion in high-entropy alloys. Figure from [owen_jones_2018]	8
3.1	PDFs of (a) 20 and (b) 250 atom SQS models of CrFeMnNi [heav2016_ch10]	13
3.2	Density of states with SQS and MC/MD of FCC CoCrFeNi, figure from [heav2016_ch10]	14
3.3	Probability distribution functions with SQS and MC/MD of HCP CoOsReRu [heav2016_ch10]	14
4.1	Number of DFT studies per year from 1980 to 2021 [dimensions].	16
5.1	Calculated to experimental band gap measurements of Becke-Johnsoon, modified Becke-Johnson and SCAN functionals [xc_benchmark]	27
5.2	Self consistent iteration of a DFT calculation. Figure adopted from lecture notes fys-mena4111 [persson2020]	30
6.1	5 distinct 48 atom SQS of $\text{Cr}_4\text{Fe}_4\text{Mn}_4\text{Ni}_4\text{Si}_{32}$ based on the β - FeSi_2 crystal structure. Illustrated with VESTA [vesta]	33
7.1	Density of states (PBE) β - FeSi_2	37
7.2	Density of states of SQS D ($\text{CrFeMnNi})\text{Si}_2$ with PBE.	39
7.3	Density of states of SQS B ($\text{CrFeMnNi})\text{Si}_2$ with PBE.	39
7.4	Local density of states of Si (SQS D)	43
7.5	Local density of states of (a) Cr, (b) Mn, (c) Fe, (d) Ni in SQS D.	43
7.6	Projected density of states SQS D CFMN (fesi2) from PBE calculation	44
7.7	Projected density of states of SQS D and B around E_F	44
7.8	Density of states illustrating the band gaps from PBE and SCAN calculations for SQS E and D.	46
7.9	Density of states of SQS B with HSE06	46
7.10	Pair distribution functions of SQS D (top) and B (bottom) . . .	50
7.11	Charge density in SQS A, B, D and E of $\text{Cr}_4\text{Fe}_4\text{Mn}_4\text{Ni}_4\text{Si}_{32}$. . .	51
7.12	CPU time of 48, 96 and 192-atom SQSs of ($\text{CrFeMnNi})\text{Si}_2$. . .	52
7.13	Density of states of SQS E 192 atom SQS.	54

7.14	Pair distribution functions of $(\text{CrFeMnNi})\text{Si}_2$ (top) 48-atom SQS, (middle) 96-atom SQS, (bottom) 192-atom SQS.	55
8.1	Projected density of states of (a) $\text{Cr}_3\text{Fe}_3\text{Mn}_7\text{Ni}_3\text{Si}_{32}$ (SQS B), (b) $\text{Cr}_5\text{Fe}_5\text{Mn}_3\text{Ni}_3\text{Si}_{32}$ (SQS C), (c) $\text{Cr}_5\text{Fe}_3\text{Mn}_5\text{Ni}_3\text{Si}_{32}$ (SQS A), (d) $\text{Cr}_3\text{Fe}_5\text{Mn}_5\text{Ni}_3\text{Si}_{32}$ (SQS D)	58
8.2	Projected density of states of $\text{Cr}_3\text{Fe}_3\text{Mn}_3\text{Ni}_7\text{Si}_{32}$ around E_F	59
8.3	Projected density of states of $(\text{CrFeMnCo})\text{Si}_2$	63
8.4	Projected density of states	63
8.5	Density of states of two SQS A and E of $(\text{CoFeMnNi})\text{Si}_2$	64
A.1	Density of states SQS A ($\text{CrFeMnNi})\text{Si}_2$ with PBE.	68
A.2	Density of states SQS E ($\text{CrFeMnNi})\text{Si}_2$ with PBE.	69
A.3	Density of states SQS C ($\text{CrFeMnNi})\text{Si}_2$ with PBE. Nedos represent the number of points in the DOS calculation.	69
A.4	Projected density of states SQS A	70
A.5	Projected density of states SQS B	70
A.6	Projected density of states SQS E	71
A.7	Charge density of SQS C.	71
B.1	Density of states SQS C $\text{Cr}_5\text{Fe}_5\text{Mn}_3\text{Ni}_3\text{Si}_{32}$, illustrating the small finite DOS at E_F due to the impurity gap.	72

List of Tables

7.1	Total energy per atom, final magnetic moment and band gap of 5 unique SQS of $(\text{CrFeMnNi})\text{Si}_2$ based on the $\beta-\text{FeSi}_2$ unit cell.	37
7.2	Band gap of the 5 SQSs of $(\text{CrFeMnNi})\text{Si}_2$ calculated from the eigenvalues in spin up, down and total.	40
7.3	Band gap of SQS D as a function of occupancy in the eigenvalues.	41
7.4	Band gap calculated with PBE, SCAN and HSE06 XC-functionals of $(\text{CrFeMnNi})\text{Si}_2$ SQSs.	45
7.5	Minimum gap between k-point in valence band and conduction band in SQS B from PBE, SCAN and HSE06	47
7.6	Band gap from HSE06 calculations with Gaussian smearing and smearing width <i>sigma</i> equal to 0.05 and 0.005, and the tetrahedron method (TBC). "-" means unchanged	48
7.7	Total energy, magnetic moment and formation energy of 48, 96 and 192 atom SQSs of $(\text{CrFeMnNi})\text{Si}_2$	52
7.8	Band gap of SQSs of 48, 96 and 192-atoms of $(\text{CrFeMnNi})\text{Si}_2$. The names are arbitrary, ie A in 48 does not equal A in 96 or A in 192. The values listed in <i>cursive</i> indicate a defect band gap.	53
8.1	Summary composition diagram	56
8.2	Band gaps of various compositions of $(\text{CrFeMnNi})\text{Si}_2$. Most stable SQS of a set is highlighted in bold text, defect/impurity band gap are listed in <i>cursive</i> . Some SQSs were excluded from the table due to unsuccessful calculations.	57
8.3	Overview new compositions	60
8.4	Final magnetic moment of the utmost stable SQS of each composition.	61
8.5	The band gap in spin up/down and total of the utmost stable SQS in five high-entropy silicides based on $\beta\text{-FeSi}_2$	62

Preface

Gotta give a shout out for my mans Jens

Chapter 1

Introduction

some introduction on the importance of discovering new materials and alloying.

Need something on thermoelectricity related to both the band gap and high-entropy alloys.

High-entropy alloys is a novel class of materials based on alloying multiple components, as opposed to the more traditional binary alloys. This results in an unprecedented opportunity for discovery of new materials with a superior degree of tuning for specific properties and applications. Recent research on high-entropy alloys have resulted in materials with exceedingly strong mechanical properties such as strength, corrosion and temperature resistance, etc **find references**. Meanwhile, the functional properties of high-entropy alloys is vastly unexplored. In this study, we attempt to broaden the knowledge of this field, the precise formulation of this thesis would be an exploration on the possibilities of semiconducting high-entropy alloys.

A key motivation of this thesis is the ability to perform such a broad study of complex materials in light of the advances in material informatics and computational methods. In this project, we will employ Ab initio methods backed by density functional theory on top-of the line supercomputers and software. 20 years ago, at the breaking point of these methods, this study would have been significantly narrower and less detailed firstly, but secondly would have totaled ... amount of CPU hours to complete (**Calculate this number**). In the addition to the development in computational power, is also the progress of modeling materials, specifically we will apply a method called Special Quasi-random Structures (SQS) to model high-entropy alloys or generally computationally complex structures. Together with the open landscape of high-entropy alloys described above, these factors produce a relevant study in the direction of applying modern computational methods to progress the research of a novel material class and point to promising directions for future research.

In specifics, this thesis revolve around the electrical properties of high-entropy alloys, mainly the band gap as this is the key indicator for a semiconducting material and it's applicability. Semiconductors are the building blocks in many different applications in today's world, ranging

from optical and electrical devices, to renewable energy sources such as solar and thermoelectricity. Given the economic and sustainable factors concerning silicon, in addition to its role in relevant applications such as microelectronics and solar power. Silicon emerges as a natural selection to build our alloys around. Furthermore, the development and research on both high entropy alloys and metal silicides have been heavily centered around 3d transition metals. Keeping in line with the economic and environmental factors, we will continue this direction by focusing on high entropy stabilized sustainable and economic 3d metal silicides **Not happy with this writing**. Throughout the study we will analyze a great number of permutations of 3d silicides, from different initial metal silicides such as $CrSi_2$, $FeSi_2$, $MnSi_{1.75}$, Fe_2Si , each with distinct properties relating to the band gap, crystal structure and metal to silicon ratio. In addition, the permutations include numerous metal distributions and elements within the 3d-group of metals. Examples are Co, Cr, Fe, Mn, and Ni.

Given a background in high-entropy alloys, one could ask if this study is truly sensible. In the later sections we will cover the details of this field, and it quickly become clear that the materials investigated in this study does not fall under the precise definition of high-entropy alloys, nor do we intend to explore the properties and factors relating to high-entropy stabilized alloys such as the configurational entropy, phase stability and finite temperature studies. However this study is motivated from the discovery of these materials and promising properties, and venture into a more hypothetical space of materials, enabled by the computational methods available to study the potential properties of such materials. On the other hand, very recent studies **Mari, and other HEA silicide study** have experimentally synthesized high-entropy disilicides, thus in some way justifying the direction of this project.

We begin this project by reviewing key concepts of solid-state physics for readers lacking a background in materials science, and an introduction to the base 3d silicides of the experimental work. Later follows a theoretic walk-through of the relevant concepts of this thesis, these topics include high-entropy alloys, special quasi-random structures, and density functional theory. Next we shine light on the implementation of DFT in this project, and other computational details required to reproduce the results in this thesis, such as the use of the Vienna Ab Initio Simulation Package (VASP) and implementation of SQS. Finally we present the results of our study, these include the band gap and electronic properties of various structures and the success and challenges of the computational methods applied throughout the study.

Part I

Theory

Part II

Method

Part III

Results and Discussion

Chapter 7

The high-entropy silicide $(\text{CrFeMnNi})\text{Si}_2$

7.1 Bulk β - FeSi_2

We begin by presenting a brief overview of the parent compound β - FeSi_2 that we have used as a foundation in this project.. In addition this is the sole case in this project where our methods and results can be compared to experimental work and relevant literature.

β - FeSi_2 is a well known semiconductor with an experimentally measured band gap of around 0.85 eV at room temperature [1]. The nature of the band gap is under debate, all though most ab initio studies result in an indirect gap, experimental studies agree on a direct band gap. From our own calculations we get an indirect band gap of 0.65 eV with PBE GGA functional. In comparison materials project list a band gap of 0.70 eV with the same functional. This slight discrepancy is most likely down to use of different parameters in the calculations, for example the cutoff energy or number of k-points. In agreement with materials project our calculations return a final magnetic moment of the compound equal to 0, this can be seen in the electronic density of states of the material plotted in figure 7.1, by that the DOS and hence band gap is identical in both spins.

The formation energy E_{form} of the compound can be calculated as the difference in total energy between the product and the sum of reactants. For the FeSi_2 compound that consist of 16 iron atoms and 32 silicon we get

$$E_{\text{form}} = -327.72\text{eV} - (16 \times -8.32\text{eV} + 32 \times -5.42\text{eV}) = -21.16\text{eV},$$

or formation energy per atom $E_{FPA} = 0.441\text{eV}$ from $-21.16/48$. The total energy of iron and silicon was calculated separately for the respective base elements with identical parameters as used for the FeSi_2 calculation. The total energies correspond well with the listed energies from materials project of -8.4693 eV and -5.4234 eV for Fe and Si respectively. Accordingly the formation energy per atom for β - FeSi_2 of 0.441 eV is in good agreement with materials project's value of 0.444 eV for β -. Again, the

difference is most likely related to materials project utilizing a larger energy cutoff of 520 eV compared to our value of 300 eV.

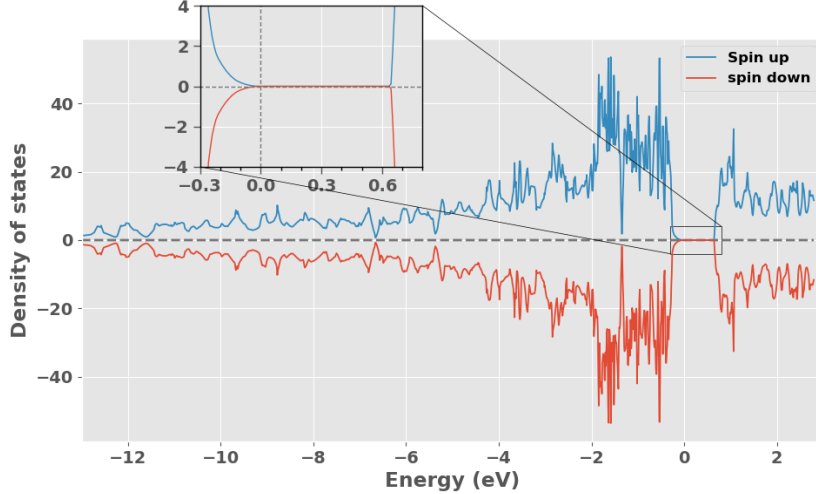


Figure 7.1: Density of states (PBE) β - FeSi₂

7.2 (CrFeMnNi)Si₂ SQSs

Below in table 7.1 we list the total energy per atom (Toten), final magnetic moment per atom (Mag) and band gap (E_G) of five unique SQSs of the Cr₄Fe₄Mn₄Ni₄Si₃₂ alloys based on the β - FeSi₂ structure. In addition we include the mean and standard deviation (std) between the 5 supercells and the formation energy calculated from the mean total energy. Details on the generation and general features of the SQSs are provided in section 6.2.

SQS	Toten (eV)	Mag (μ_B)	E_G (eV)
A	-6,6080	0.0833	0.0280
B	-6,6138	0.0833	0.0523
C	-6,6063	0.0834	0.0344
D	-6,6155	0.0833	0
E	-6,6089	0.0833	0.0495
Mean	-6.6105	0.0833	0.0328
Std	0.0039	0.0000	0.0210
E_{FPA} (eV)	-0.293	-	-

Table 7.1: Total energy per atom, final magnetic moment and band gap of 5 unique SQSs of (CrFeMnNi)Si₂ based on the β - FeSi₂ unit cell.

From table 7.1 we observe that the total energy and magnetic moment are quite similar in all 5 supercells, which could be expected from that the atomic configuration is the only variable. On the other hand the atomic

configuration have a larger impact on the band gap of the supercells. We find that the band gap ranges from a maximum value of 0.05 eV in SQS B, to a metal in SQS D, nevertheless much smaller than FeSi_2 (0.65 eV). We will come back to discussing the band gaps in later sections.

Compared to the bulk material we find that the alloy apparent from all five supercells display a finite magnetic moment of around $0.083\mu_B$. The local magnetic moments show some variation between supercells but follow the same trend where the largest moments are attributed to chromium atoms in the lattice, followed by manganese. On the other side the magnetic moments of both iron and nickel within the numerical accuracy of the calculations give negligible contributions to the magnetic moment of the structures. Considering that the total magnetic moment is identical in 5 distinct atomic configurations and the local magnetic moments show very similar trends, the observed magnetism within the scope of this project is most probably connected to the particular crystal structure. It should be noted however that the magnetic properties in this project could be prone to errors. As we discussed in section 4.3 one of the major drawbacks of DFT in regards to magnetic materials is the local minima problem. In this project we have overlooked this concern and applied a constant initial co-linear magnetic configuration in all structures in order to reduce the workload, thus it's possible that the final magnetic structure of the supercells adopt local minimas rather than global. Coupling this with the possible errors associated with the special quasi-random structures method to model the disordered magnetic structure means that the magnetic results and following the total energy and corresponding stability are not immutable nor necessarily accurate in respect to the hypothetical real alloy.

In terms of the total energy the most and least stable SQSs are "D" and "A" respectively, meaning that SQS D is then the most representative configuration of the real material. However most likely all five SQSs and other possible configurations would appear as local orderings in domains of the real material with a certain probability. Therefore we will consider and discuss the results of all 5 SQSs as well as the most stable supercell. Further the total energy alone is not sufficient to evaluate the stability of the structure. In this project we have not considered factors such as the configurational entropy or made any finite temperature considerations in general. Additionally the discussion above on the magnetic configuration could affect the total energy. Thus the relative stability between supercells listed in table 7.1 could be variable, nevertheless the most stable configuration is moderately emphasized from the considerations made in this project.

7.2.1 The band gap

As seen from table 7.1 the band gap of the alloy are severely reduced from the bulk material, and vary from supercell to supercell. We observed a maximum band gap of 0.05 eV in SQS B, and on the flip side a 0 band gap in the utmost stable configuration SQS D. The density of states of SQS D and B is displayed in figures 7.2 and 7.3 below, similar plots can be found in appendix A.1 of the other SQSs.

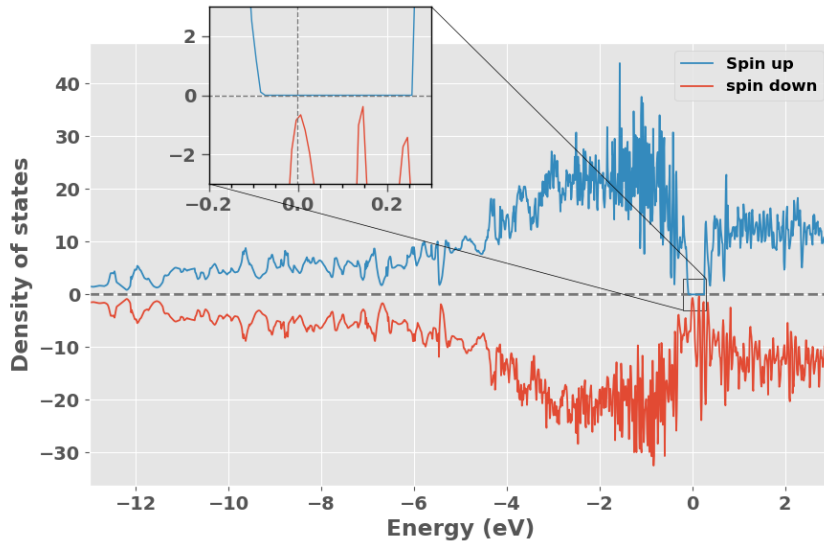


Figure 7.2: Density of states of SQS D ($\text{CrFeMnNi}\text{Si}_2$) with PBE.

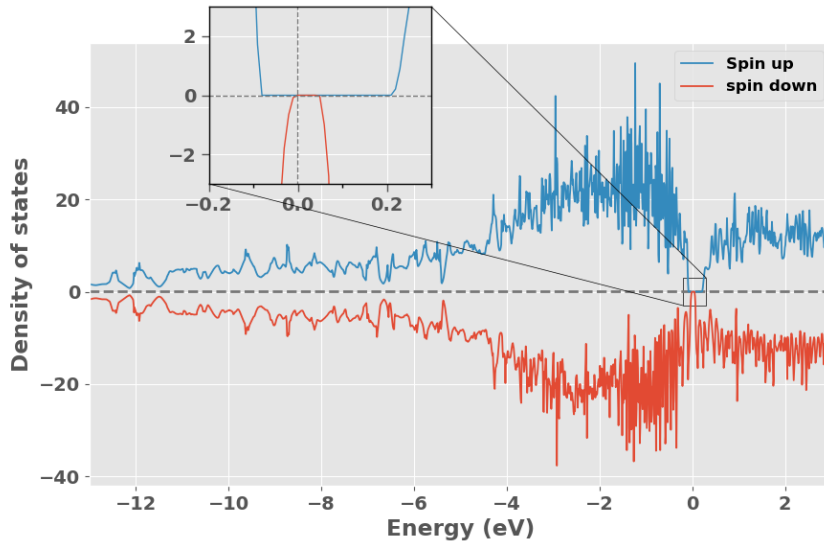


Figure 7.3: Density of states of SQS B ($\text{CrFeMnNi}\text{Si}_2$) with PBE.

In figure 7.2 and 7.3 we observe that the band gap in both SQS D and B

in accordance with the magnetic property is different between spins. Going forward we will refer to the band gap in spin up as E_G^{up} , and spin down as E_G^{dw} . Clearly in both D and B $E_G^{\text{up}} >> E_G^{\text{dw}}$ as SQS D for instance exhibits a band gap of around 0.3 eV in spin up, contrary to a 0 band gap in spin down. Comparing to the values in table 7.1 we find that the total band gaps of the respective structures is limited by the narrow or nonexistent band gap in spin down. To obtain further and more precise information on the band gap we look to the calculated Kohn-Sham eigenvalues. The eigenvalue band gaps, denoted as E_G^{eigen} can be seen below in table 7.2 for all five SQS, where the utmost stable configuration (SQS D) is highlighted in bold text. Continuing the trend described above we observe equivalent to SQS D and B that $E_G^{\text{up}} >> E_G^{\text{dw}}$ for all supercells, par SQS A where the spin polarization of the band gap is less prominent and the total band gap is the combined sum of E_G^{up} and E_G^{dw} .

SQS	$E_G^{\text{up, eigen}}$ (meV)	$E_G^{\text{dw, eigen}}$ (meV)	$E_G^{\text{tot, eigen}}$ (meV)
A	81.4	52.2	28.1
B	293	52.2	52.2
C	236	34.3	34.3
D	339	0.00	0.00
E	308	50.0	50.0

Table 7.2: Band gap of the 5 SQSs of (CrFeMnNi)Si₂ calculated from the eigenvalues in spin up, down and total.

In VASP the energy eigenvalues are listed for every energy band at all k-points used in the calculation, with corresponding occupancy. An occupancy of 1 represents a fully occupied eigenstate, in analog a completely unoccupied (empty) eigenstate have occupancy equal to 0. Recalling that occupied states belong to the valence band, and the conduction band consists of unoccupied states (at 0 K). The highest energy valence band in these structures are band 124 in spin down and 128 in spin up, following the lowest energy valence band is 125/129 in spin down/up. The band gap in spin down is then determined from the difference between the lowest energy eigenvalue in band 125 and the highest energy eigenvalue in band 124, and likewise for the spin up band gap between bands 128 and 129. In SQS D different from the semiconducting structures we observe some partially occupied states at the band edges in bands 124 and 125 in spin down. With partially occupied states we refer to eigenstates in the valence band with occupancy less than 1 and states in the conduction band with occupancy above 0. Specifically the highest energy eigenvalue (9.01 eV) in band 124 have occupancy equal to 0.94, and equivalently the lowest energy eigenvalue (8.98 eV) in band 125 have occupancy equal to 0.08. This results in a 0 (negative) band gap. Further the Fermi energy in this structure is 8.99 eV, the partially occupied eigenstate in band 124 is then above the Fermi energy, and the partially unoccupied eigenstate in

the conduction band below the Fermi energy. This is a clear indication of a metal, in which the conduction band and valence band overlap. In this project we will refer to such eigenstates with partial occupancy as defect states. The importance of the defect states on the band gap in SQS D can be seen clearly in table 7.3. Here we calculate the band gap as a function of the defect states by an occupancy parameter occ , such that $E_G(0.99, 0.01)$ is the band gap when only including eigenvalues with corresponding occupancy above 0.99 in the valence band and below 0.01 in the conduction band. For simplicity we will write the parameter as a single value, where $occ = 0.01$ represents occupancy equal to 1 - 0.01 in the valence band and 0 + 0.01 in the conduction band.

occ	$E_G^{\text{up, eigen}}$ (meV)	$E_G^{\text{dw, eigen}}$ (meV)	$E_G^{\text{tot, eigen}}$ (meV)
0.5	339	0	0
0.05	339	21.0	21.0
0.01	339	49.6	49.6
0.001	339	73.3	73.3
<0.0001	339	85.7	85.7

Table 7.3: Band gap of SQS D as a function of occupancy in the eigenvalues.

From table 7.3 we find clear evidence of the defect states prohibiting the band gap in spin down in SQS D, compared to the semiconducting supercells that contain only fully occupied and unoccupied eigenstates. To investigate this effect to greater extent we compare the eigenvalues of SQS D to a pure metal, such as iron. In this case the energy bands (both spins) around the Fermi energy (5.8 eV) is populated mostly by partially filled eigenstates. Inside a single energy band we observe instances of both more than half-filled states above E_F , and less than half-filled states above E_F , thus clearly overlap between the conduction and valence band. In contrast we find no instances of partial occupants in pure Si, as in the semiconducting SQSs. Therefore we can firmly state that the "defect states" are associated with a metallic character. Compared to the pure metal however, the amount and severity of the partial occupants are very dampened in SQS D. The concept of defect or impurity states in the band gap have been found as a common feature of the band structure of random alloys [2], however we have reservations about if this is a physical result or related to numerical factors. In addition to partial occupants in Fe and SQS D we observe a plural of non-naturalistic states where the occupancy exceeds 1 and 0. Recalling that the discontinues Fermi surface of metals poses several obstacles on DFT calculations with respect to the smearing and number of k-points. This result could then be imagined as a consequence of numerical methods. For instance in SQS B we conducted three separate electronic calculations, one with the tetrahedron method (value listed in tables) and two calculations with Gaussian smearing with smearing width 0.05 and 0.005 eV. With the Gaussian method and smearing

width $\sigma = 0.05\text{eV}$ we get $E_G^{\text{up, eigen}} = 0.2987\text{eV}$ and $E_G^{\text{dw, eigen}} = 0.0497\text{eV}$. Further calculations with the Gaussian method with smearing width of 0.005 eV results in $E_G^{\text{up, eigen}} = 0.2932\text{eV}$ and $E_G^{\text{dw, eigen}} = 0.0522\text{eV}$. Compared to the values in table 7.3 with TBC, we observe that Gaussian (0.005 eV) and TBC are identical, while Gaussian (0.05 eV) show some deviation. Furthermore we find that the eigenvalues of Gaussian 0.05 eV contain defect states, and that the spin down band gap can thus be enlarged as in SQS D previously by $E_G^{\text{dw, eigen}}(0.01) = 0.1695\text{eV}$. However, in this case we find no instances of non-naturalistic states as we described above for SQS D with TBC.

In conclusion, the defect states observed in SQS D is clearly related to a metallic structure, however from the discussion above we have seen that the results could be subject to numerical factors as well. It would have been instructive to visualize and analyze the eigenvalues by plotting the band structure. Unfortunately this is neither simple to perform or interpret for large supercells consisting of several elements and a large number of energy bands. One solution could be band-unfolding, but this did not work in conjunction with the implementation of the SQS method in this project.

7.2.2 Local and projected density of states

In this section we will analyze the local and projected density of states of primarily SQS D (most stable). Below we include the local density of states of silicon in figure 7.4, and the respective LDOS plots of the various 3d elements of the compound in figure 7.5.

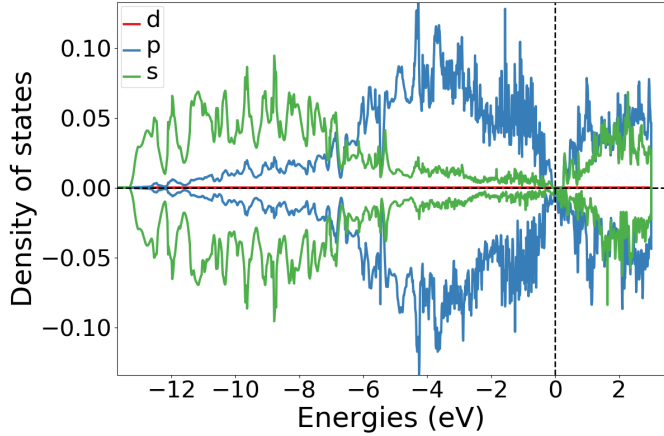


Figure 7.4: Local density of states of Si (SQS D)

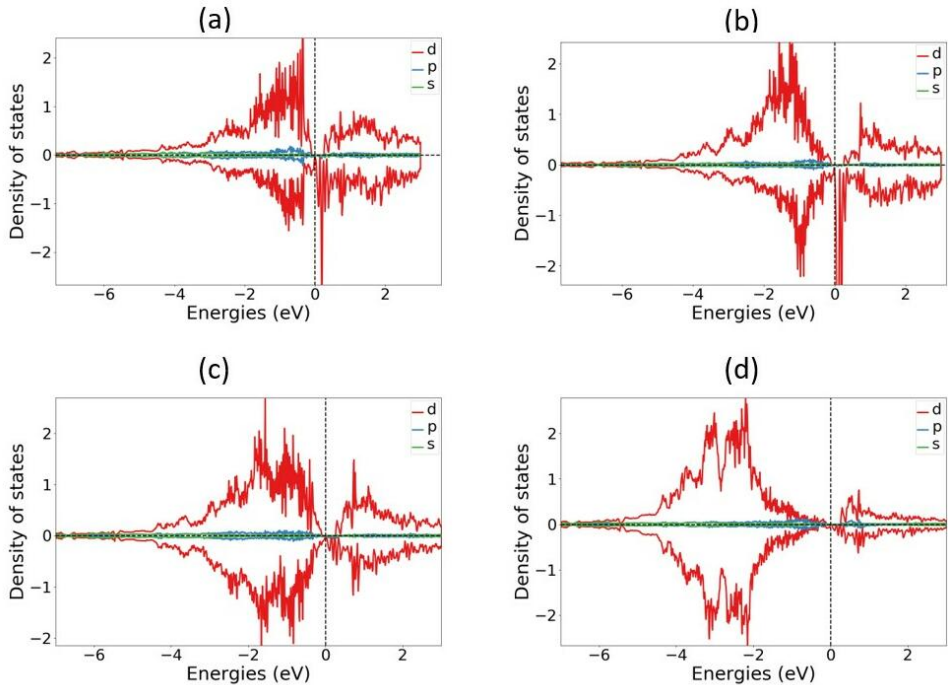


Figure 7.5: Local density of states of (a) Cr, (b) Mn, (c) Fe, (d) Ni in SQS D.

In the local density of states plotted in figure 7.4 we see that the s-electrons in Si occupy states in the lower energy regions and p electrons at slightly elevated energies closer to the Fermi energy. Above E_F states

are occupied by s and p electrons equally. Between the 3d electrons of the transition metals, markedly manganese and chromium display a strong presence at energies just above E_F and manganese additionally below E_F . Iron and Nickel show largest contributions at energies further from the Fermi energy, most notably below E_F . In the spin up channel we see a similar trend where chromium lie closest to E_F followed by manganese, iron and lastly nickel at the lowest energies. It could also be noted that in relation to the local magnetic moments discussed previously, we observe that the local density of states is symmetric with respect to spin in Fe and Ni, but not in Cr and Mn.

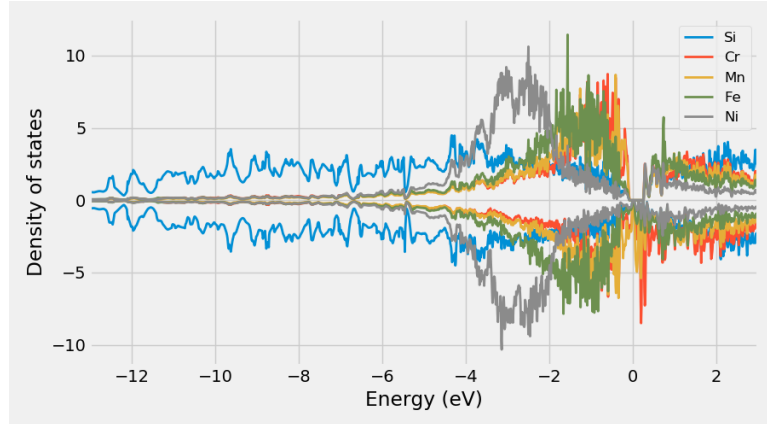


Figure 7.6: Projected density of states SQS D CFMN (fesi2) from PBE calculation

The interplay between 3d elements and silicon as shown in the projected density of states (figure 7.6) is in good agreement with observed trends in simpler Si-rich transition metal silicides [3] and Fe and Si β –FeSi₂ [4].

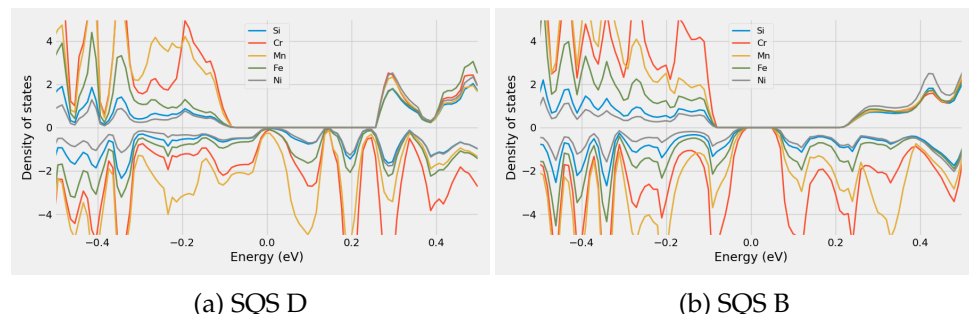


Figure 7.7: Projected density of states of SQS D and B around E_F

Comparing the PDOS of half-metallic SQS D (figure 7.7 a) to the configuration with the largest E_G^{dw}) SQS B (figure 7.7 b), we find distinctly a large number of Mn states in SQS D around E_F most noticeably in spin down, but also in spin up. The PDOSs of SQSs A, B, and E are included in appendix A.2 (unable to plot PDOS for SQS C)

7.2.3 The band gap with SCAN and HSE06

As expressed previously, in this work we invoke 3 level of depths GGA (PBE), meta-GGA (SCAN) and hybrid functional (HSE06) to determine the band gap. The outcome of these 3 functionals are showcased in table 7.4.

SQS	XC-functional	E_G^{up} (eV)	E_G^{dw} (eV)	E_G^{tot} (eV)
A	PBE	0.0815	0.0521	0.0281
	SCAN	0	0	0
	HSE06	0.7084	0.0261	0.0261
B	PBE	0.2932	0.0523	0.0523
	SCAN	0.1470	0.0890	0.0890
	HSE06	0.2855	0.1819	0.1819
C	PBE	0.2355	0.0343	0.0343
	SCAN	0.0690	0.1124	0.1124
	HSE06	0.1744	0.0328	0.0196
D	PBE	0.3386	0	0
	SCAN	0	0.1086	0
	HSE06	0.3780	0	0
E	PBE	0.3078	0.0495	0.0495
	SCAN	0.1540	0.1112	0.1048
	HSE06	0.5476	0.0133	0.0133

Table 7.4: Band gap calculated with PBE, SCAN and HSE06 XC-functionals of $(\text{CrFeMnNi})\text{Si}_2$ SQSs.

We will begin dissecting table 7.4 by comparing SCAN to PBE. The first distinction we make notice of is in SQS A. In this supercell calculations with the SCAN functional predicts a metallic compound, contrary to the the PBE band gap of 0.03 eV. Alike the band gap of SQS D discussed previously, the 0 band gap in this structure with SCAN is caused by defect states. Neglecting such states and evaluating the band gap from just completely filled and empty eigenstates yield $E_{G, \text{SCAN}}^{\text{up}, \text{eigen}}(0.99, 0.01) = 0.0316$ eV and $E_{G, \text{SCAN}}^{\text{dw}, \text{eigen}}(0.99, 0.01) = 0.0531$ eV, and a total band gap of 0.0316 eV. This value seems to agree better with the PBE band gap of this supercell, but we observe that E_G^{up} is larger in PBE. This is a recurrent patter with SCAN across all five SQSs, where $E_{G, \text{SCAN}}^{\text{up}} < E_{G, \text{PBE}}^{\text{up}}$, and moreover $E_{G, \text{SCAN}}^{\text{dw}} > E_{G, \text{PBE}}^{\text{dw}}$. This can be seen in figure 7.8, where we plot the density of states of SQS E (a, b) and C (c, d). Note that the SCAN band gap in SQS C have the opposite spin polarization of PBE, this is also the case in SQS D as seen from table 7.4.

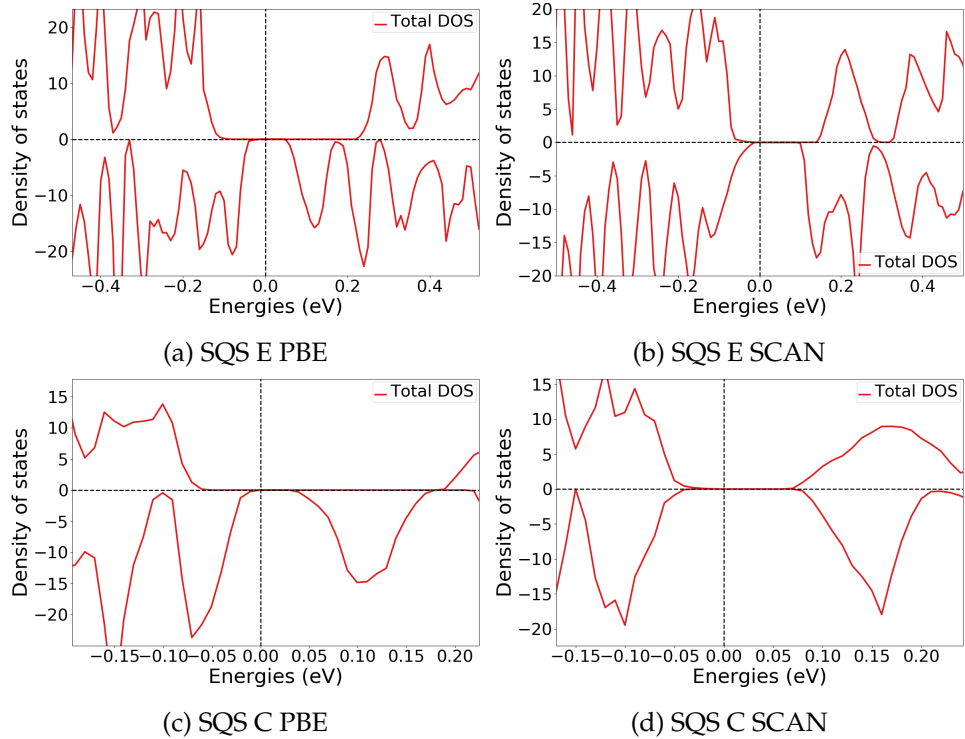


Figure 7.8: Density of states illustrating the band gaps from PBE and SCAN calculations for SQS E and D.

With the HSE06 functional we observe the opposite trend to SCAN in SQS A and E, where $E_{G, \text{HSE06}}^{\text{up}} > E_{G, \text{PBE}}^{\text{up}}$ and $E_{G, \text{HSE06}}^{\text{dw}} < E_{G, \text{PBE}}^{\text{dw}}$. But in other cases $E_{G, \text{HSE06}}^{\text{up}}$ is lesser (SQS C) or similar to PBE (SQS B and D). On the other hand $E_{G, \text{HSE06}}^{\text{dw}}$ is consistently smaller in all structures compared to PBE, with the exception of SQS B. In this structure the HSE06 functional predicts large band gaps in both spins, as seen from the density of states plotted in figure 7.8.

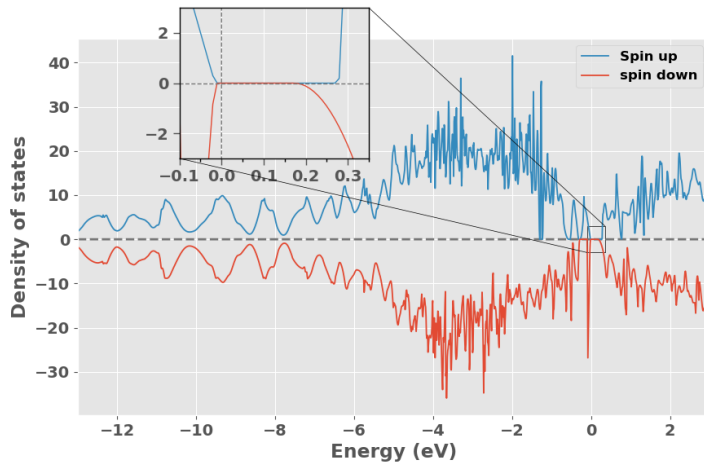


Figure 7.9: Density of states of SQS B with HSE06

As we discussed in section 5.1, hybrid functionals are much more computationally demanding compared to both meta-GGA and GGA functionals. In this project we experienced particular difficulty of converging calculations with HSE06 of the compositionally complex structures. To reduce the cost of the HSE06 functional we performed such calculations with a lower density of k-points, see section 6.1. The small amount of k-points could as discussed lead to numerical inaccuracies relating to the calculation of the Fermi surface in metallic structures. Furthermore the reduced mesh of k-points could result in artificially exaggerated band gaps from failing to encapsulate the exact minimum transition between the valence band and conduction band.

XC-functional	Transition (k-point)
PBE	(0.250,0.000,0.250) → (0.000,0.000,0.000)
SCAN	(0.250,0.000,0.250) → (0.000,0.333,0.000)
HSE06	(0.500,0.000,0.000) → (0.000,0.000,0.000)

Table 7.5: Minimum gap between k-point in valence band and conduction band in SQS B from PBE, SCAN and HSE06

In table 7.5 we list the transition between the highest occupied k-state in the valence band and lowest unoccupied k-state in the conduction band for SQS B with PBE, SCAN and HSE06 respectively. We observe that all 3 functionals find different band gaps. A concerning factor is that the highest energy k-point in the valence band from PBE calculations (0.250, 0.000, 0.250) is not included in the HSE06 calculation with the narrow mesh of 2x2x2 k-points. Thus one may suspect that the HSE06 calculation overlook the minimum transition and hence return a enlarged band gap instead. This could be the case in $E_{G,A}^{up}$ and $E_{G,B}^{dw}$ where HSE06 predicts much larger values to PBE. However without an experimental baseline we can not conclude that this is the case. As in the other instances we find that HSE06 produce similar or lower band gaps compare to PBE despite of the smaller number of k-points.

As stated in section 6.2, we did not manage to converge hybrid calculations with the tetrahedron method, and overcame this problem by first calculating the charge density with Gaussian smearing and utilize the density to expedite TBC HSE06 calculations. The respective band gaps from these methods are displayed in table 7.6 for the five SQSs of the (CrFeMnNi)Si₂ system. Here we calculate the band gap from the eigenvalues at different cutoff occupancy *occ* to highlight the part of defect states. Gaussian smearing was tested with smearing width *sigma* equal to 0.05 eV and 0.005 eV.

SQS	Smearing (type)	$E_G^{up,eigen}$ (0.5) (eV)	$E_G^{down,eigen}$ (0.5) (eV)	$E_G^{up,eigen}$ (0.99) (eV)	$E_G^{down,eigen}$ (0.99) (eV)	$E_G^{tot,eigen}$ (0.01) (eV)	$E_G^{tot,eigen}$ (0.5) (eV)	$E_G^{tot,eigen}$ (0.99, 0.01) (eV)
A	Gaussian (0.05)	0.7837	0.1493	-	0.2984	0.1493	0.2984	
	Gaussian (0.005)	0.2117	0.1013	-	-	0.1013	-	
	TBC	0.7084	0.0261	-	-	0.0261	-	
B	Gaussian (0.05)	0.2783	0.1702	0.2988	0.3136	0.1506	0.2979	
	Gaussian (0.005)	0.2838	0.1823	-	-	0.1801	-	
	TBC	0.2855	0.1819	-	-	0.1807	-	
C	Gaussian (0.05)	0.1078	0.1066	0.2405	0.1839	0.0650	0.1839	
	Gaussian (0.005)	0.1304	0.0222	-	-	0.0222	-	
	TBC	0.1744	0.0328	-	-	0.0196	-	
D	Gaussian (0.05)	0.3661	0.0592	-	0.1872	0.0592	0.1872	
	Gaussian (0.005)	0.3736	0.0723	-	-	0.0723	-	
	TBC	0.3780	0	-	0.2665	0	0.2637	
E	Gaussian (0.05)	0.6653	0.1439	-	0.1675	0.1439	0.1675	
	Gaussian (0.005)	0.5825	0.1211	-	-	0.1211	-	
	TBC	0.5476	0.0133	-	-	0.0133	-	

Table 7.6: Band gap from HSE06 calculations with Gaussian smearing and smearing width σ equal to 0.05 and 0.005, and the tetrahedron method (TBC). "-" means unchanged

From table 7.6 we observe that the presence and affect of defect states as discussed in section 7.2.1 is only present with Gaussian ($\sigma = 0.05\text{eV}$). Alike the previous cases, we find here finite band gaps despite of defect states. By comparing E_G^{up} and E_G^{dw} at $occ = 0.5$ and $occ = 0.01$, the defects appear to have a lesser role in spin up, as par SQS C the band gap in spin up is either consistent or only marginally different between the defect band gap and the hypothetical defect less band gap. E_G^{dw} on the other hand increase significantly by removing the defect states. The Gaussian smearing method is generally in better agreement with TBC at lower smearing width. But even in this case we find several dissimilarities. In A and E E_G^{dw} is larger with the Gaussian method, additionally E_G^{up} is much lower in SQS A. Furthermore the band gap of SQS D with HSE06 is with TBC in good agreement with the half-metallic compound found with PBE, meanwhile the Gaussian method ($\sigma = 0.005\text{eV}$) predicts a semiconductor with band gap equal to 0.07eV . In this project we have based our choice of numerical smearing on the advice on the VASP manual that state that for accurate total energies and density of states in semiconductors one should opt for the tetrahedron method [5]. However since our system is comprised of metals as well as Si, we include the results from utilizing Gaussian smearing. There are of course many more factors that affect the accuracy and reliability of both methods, but these are outside the scope of this project.

The fact that all 3 functionals and five SQS in majority agree on the presence of a band gap is in itself an overwhelmingly positive result that allow us to state with high certainty that the potential high-entropy silicide $(\text{CrFeMnNi})\text{Si}_2$ is in fact a semiconductor or possibly a half-metal based on the observed spin polarization and the utmost stable configuration. Regarding the 3 functionals applied in this project, we experience best cohesion between PBE and HSE06 that both agree on a spin up polarization of the band gap, while SCAN predicts more symmetric band gaps. This can also be seen from the magnetic moment, with PBE and HSE06 the final magnetic moment (per atom) is $0.083 \mu_B$ across all SQSs, with SCAN this is reduced to half the amount. In the nonmagnetic β - FeSi_2 structure we find better agreement between PBE and SCAN. Both correctly predict that the material is nonmagnetic, however compared to the experimental value of about 0.85 eV and the PBE band gap of 0.65 eV , we get a smaller band gap of 0.61 eV with SCAN. Thus the SCAN functional does not necessarily result in increased accuracy over PBE even in the nonmagnetic material. To conclude this section on the band gap $(\text{CrFeMnNi})\text{Si}_2$, when studying the band gap with DFT, particularly PBE is well known to underestimate the band gap of the real material as in FeSi_2 . Therefore a band gap found with PBE would with high probability be replicated/increased in the real material. In the following sections and cases we will heavily emphasize the PBE functional to determine the band gap from both the fast and reliable use in addition to the point mentioned above. Furthermore from our experiences in this project in conjunction with the lack of literary support the SCAN function look to be ill-equipped for accurate band gaps. While the HSE06 functional is often to computationally expensive and

troublesome to converge for the structures in this project.

7.2.4 Pair distribution functions

The pair distribution functions of SQS D and B can be seen below in figure 7.10. We analyze the PDFs of the utmost stable configuration (SQS D) side by side to SQS B to investigate distinctions between the half-metallic structure and the semiconducting structure (B).

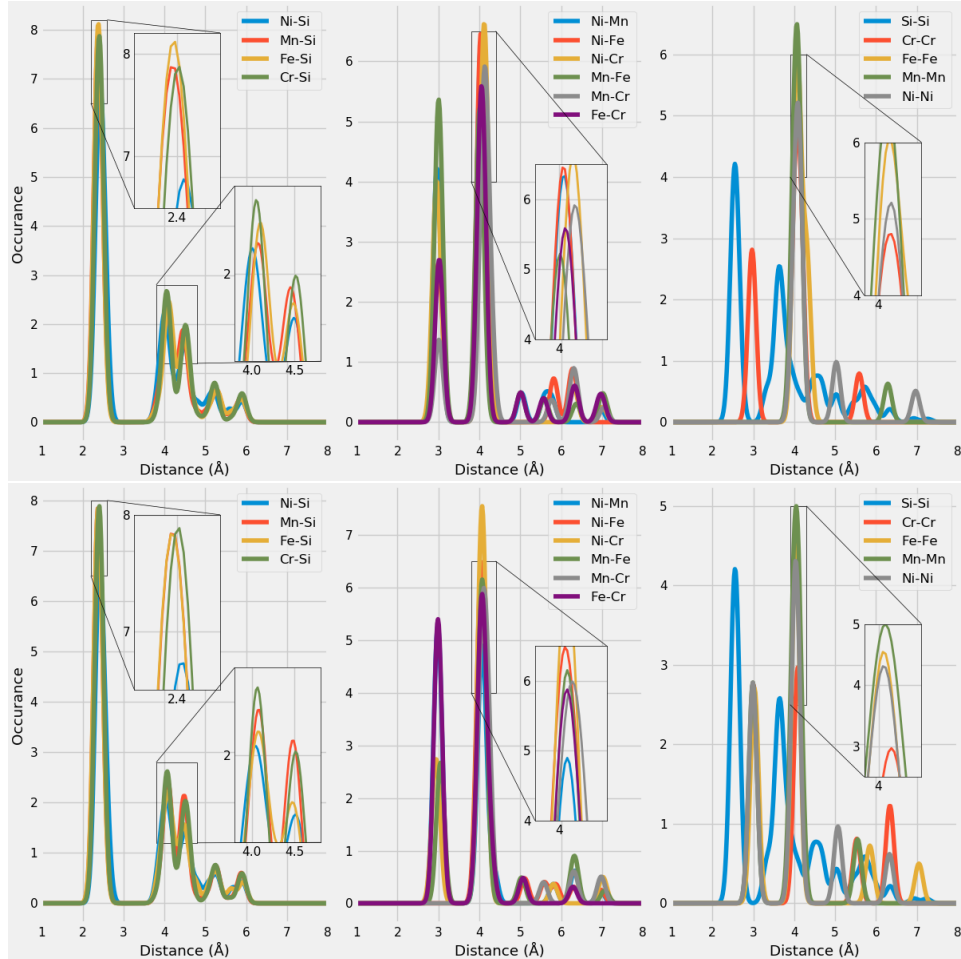


Figure 7.10: Pair distribution functions of SQS D (top) and B (bottom)

With the aid of the ICSD ([insert citation](#)), we can compare the PDFs in figure 7.10 to the expected PDFs based on a large number of experimental compounds. As our compound contain a total of 15 different bonds, comparing each one to the ICSD values would be an exhaustive process. According to the ICSD the preferred bond-length of TM-Si bonds is observed at two values, with the shorter length the most occurring. Specifically Fe-Si between 2.25-2.75 Å and 4-5 Å, Mn-Si at 2.25-2.75 Å and 3.5-5 Å, Ni-Si between 2.25-2.5 Å and 3.85-5 Å, and finally Cr-Si between 2.35-2.65 Å and 4-5 Å. Clearly, the PDFs of the SQSs are in good agreement with the listed values of TM-Si bonds. The relative occurrence of the bonds

between SQS D and B are mostly consistent, other than marginally reduced Fe-Si occurrence at 2.4 Å in B.

In contrast, we observe several distinctions between TM-TM bonds in SQS D and B, for example Mn-Fe, Cr-Fe, and Ni-Mn bonds. This is simply a consequence of how the SQSs are generated, the silicon atoms are placed as before in the new supercells, but the TM elements are "randomly" distributed. Thus, it's reasonable that we would find the major differences between TM-TM bonds. Recalling that Mn had a distinct presence in spin down around E_F in SQS D, we observe that this structure compared to SQS B have a preference of Mn-Fe bonds at 3 Å and show larger occurrence of Mn-Mn bonds at 4 Å. However the differences between PDFs are difficult to relate to the observed properties. Firstly because of the sheer number of total bonds in the structures, and secondly considering the uniqueness of each SQS paired with the uncertainties regarding the stability.

7.2.5 Charge density

Below we include the calculated charge density (with PBE) of the different configurations. The half-metallic configuration (D) appear more metallic by a greater number of delocalized electronic charges compared to the semiconducting configurations A, B, and E. The charge density of SQS C is found in appendix A.3.

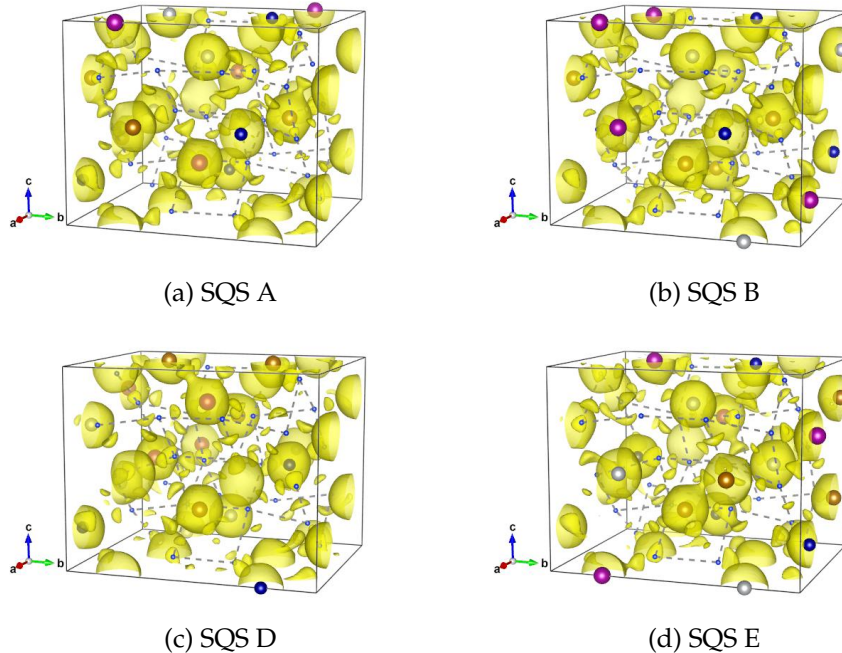


Figure 7.11: Charge density in SQS A, B, D and E of $\text{Cr}_4\text{Fe}_4\text{Mn}_4\text{Ni}_4\text{Si}_{32}$

7.2.6 SQS size

Above we have presented the results of a high-entropy silicide (CrFeMnNiSi_2) investigated by 5 48-atom SQSs with a volume of 700\AA^3 . This intermediate size allowed us to apply different XC-functionals, and a broad study of different compositions which we will discuss in the next section. However the application of the SQS method to HEAs is not necessarily straightforward as we discussed in section 4.3. The most pressing concern is the size of the SQS model and if it's sufficient enough to correctly model the disordered multi-component structure. In this section we will evaluate this factor by studying the difference between the 48 atom SQSs discussed above to that of 96 and 192-atom SQSs with volume 1200\AA^3 and 2400\AA^3 respectively. The computational cost of the 3 sizes are included below in figure 7.11 in terms of the number of CPU hours.

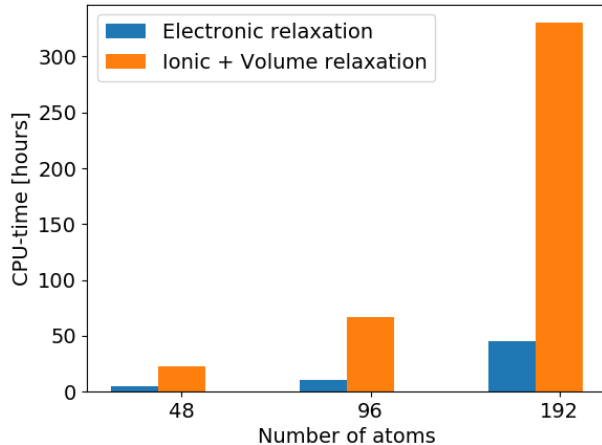


Figure 7.12: CPU time of 48, 96 and 192-atom SQSs of $(\text{CrFeMnNi})\text{Si}_2$

Alike the 48-atom model, the 96 and 192-atom SQS were tested by 5 unique configurations. In table 7.7 we report the mean and standard deviation from the set of configurations for all three sizes, with respect to the total energy per atom and final magnetic moment per atom, in addition to the formation energy of the mean total energy.

SQS size	Toten (eV)		Mag (μ_B)		E_{FPA} (eV)
	mean	std	mean	std	
48 atoms	- 6.6105	..	0.0833	0.0000	-0.292
96 atoms	- 6.6092	0.0021	0.0708	0.0114	-0.292
192 atoms	- 6.6123	0.0022	0.0761	0.0171	-0.295

Table 7.7: Total energy, magnetic moment and formation energy of 48, 96 and 192 atom SQSs of $(\text{CrFeMnNi})\text{Si}_2$

As seen from table 7.7 the total energy, magnetism and corresponding formation energy show very minimal variation between all three sizes, thus the 48-atom model is well converged. On the other hand we observe that the larger models contain larger deviation between configurations, this can be expected given the total number of atoms that can vary between configurations. The band gap corresponding to SQSs of each size are listed in table 7.8. First and foremost the band gap is evident in all three and exhibits analogous spin polarization, however the band gap appears to be less frequent and smaller in the larger structures.

SQS size	SQS	$E_G^{up,eigen}(0.5)$ (eV)	$E_G^{dw,eigen}(0.5)$ (eV)	$E_G^{tot,eigen}(0.5)$ (eV)
48 atoms	A	0.0815	0.0521	0.0281
	B	0.2932	0.0523	0.0523
	C	0.2355	0.0343	0.0343
	D	0.3386	0	0
	E	0.3078	0.0495	0.0495
96 atoms	A	0.1705	0.0442	0.0367
	B	0.1386	0.0270	0.0270
	C	0.1347	0.0363	0.0075
	D	0.0892	0.0398	0.0398
	E	0.1610	0	0
192 atoms	A	0.1197	0.0321	0.0321
	B	0.1444	0	0
	C	0.1867	0	0
	D	0.0478	0.0339	0
	E	0.0131	0.0184	0.0131

Table 7.8: Band gap of SQSs of 48, 96 and 192-atoms of $(\text{CrFeMnNi})\text{Si}_2$. The names are arbitrary, ie A in 48 does not equal A in 96 or A in 192. The values listed in *cursive* indicate a defect band gap.

Equivalent to structure D in the 48 atom SQS we find that the 0 value in SQS E in the 48 atom model suffers from defect states, and $E_G^{dw,eigen}(0.90, 0.10) = 0.016$ eV. The same is true for SQS B and C (192), but require $occ = 0.999, 0.001$ to yield a finite band gap in spin down. The band gap in SQS D and E (192) on the other hand is finite at $occ = 0.5$ but can be enlarged from increasing occ , as we described for the Gaussian ($\sigma = 0.05$ eV) calculations previously. In SQS D (192-atoms) $E_G^{up,eigen}(0.99) = 0.075$ eV and $E_G^{dw,eigen}(0.01) = 0.05$ eV and similarly $E_G^{up,eigen}(0.99) = 0.05$ eV, and $E_G^{dw,eigen}(0.01) = 0.048$ eV in SQS E (192-atoms). In such cases where the eigenvalues inclusive of defect states return a finite band gap, the density of states does not. This is seen in figure 7.12 for SQS E in the 192-atom model that clearly have nonzero DOS at E_F in both spins.

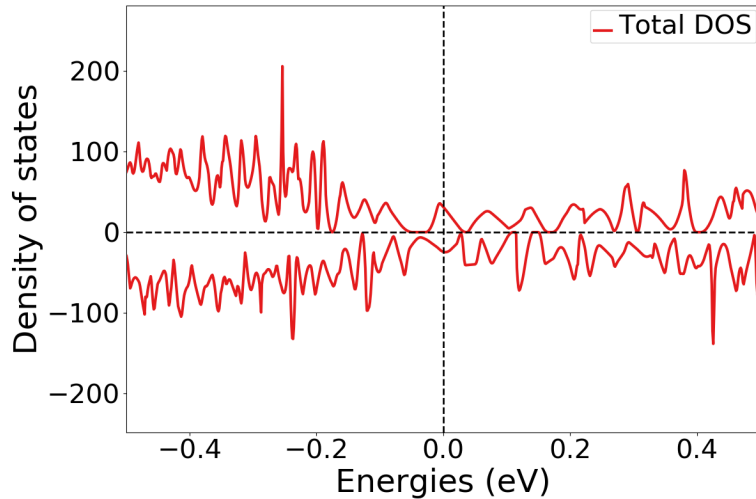


Figure 7.13: Density of states of SQS E 192 atom SQS.

One could wonder if the very narrow band gap from the eigenvalues of 0.01 eV is subject to numerical precision in the DOS. But on the grounds of the small value we calculated the DOS in this case by 20000 points over the energy range -12 eV to 12 eV which results in a resolution of about 8 points per 0.01 eV. In other words this should not be a factor of the DOS in figure 7.12.

Drawing any conclusion on the band gaps is difficult seeing as we find very different results within all 3 sizes. The utmost stable SQSs suggests that the band gap converge towards a small or possible non-existent band gap with increasing SQS size. On the other hand we also find evidence of large band gaps in the larger cells in less stable configurations. This goes back to section 3.3 where we mentioned that one particular difficulty of the SQS method is the large number of possible atomic configurations of one composition. We should note that for the sake of comparison, we conducted the calculations of the larger SQSs with identical computational parameters as the 48-atom models, this could affect the accuracy of the larger structures.

Looking at the pair distribution functions of the utmost stable SQS in each size (figure 7.13), we observe that short-range interactions is well represented and identical across all three models. The distinctions between preferences as discussed in section 7.2.4 is most likely a product of the uniqueness of the SQSs more so than the size. On the other hand the larger SQSs clearly provide a better description of large-range interactions, that is not nearly as present in the smaller supercell. But as seen from the minimal variation of the values in table 7.7 between the 3 models, in accordance with the fundamental philosophy of the SQS method that the functional properties are determined primarily from short-range interactions in the lattice. Thus, despite the fact that the larger SQSs offer improvement over the smaller SQSs, the gain is not justified by the cost. On the other hand, the SQS size looks to have more of an impact on the band gap of the material. But this could just as easily be a consequence of the sensitivity of the band

gap to the particular atomic configuration as seen in table 7.8.

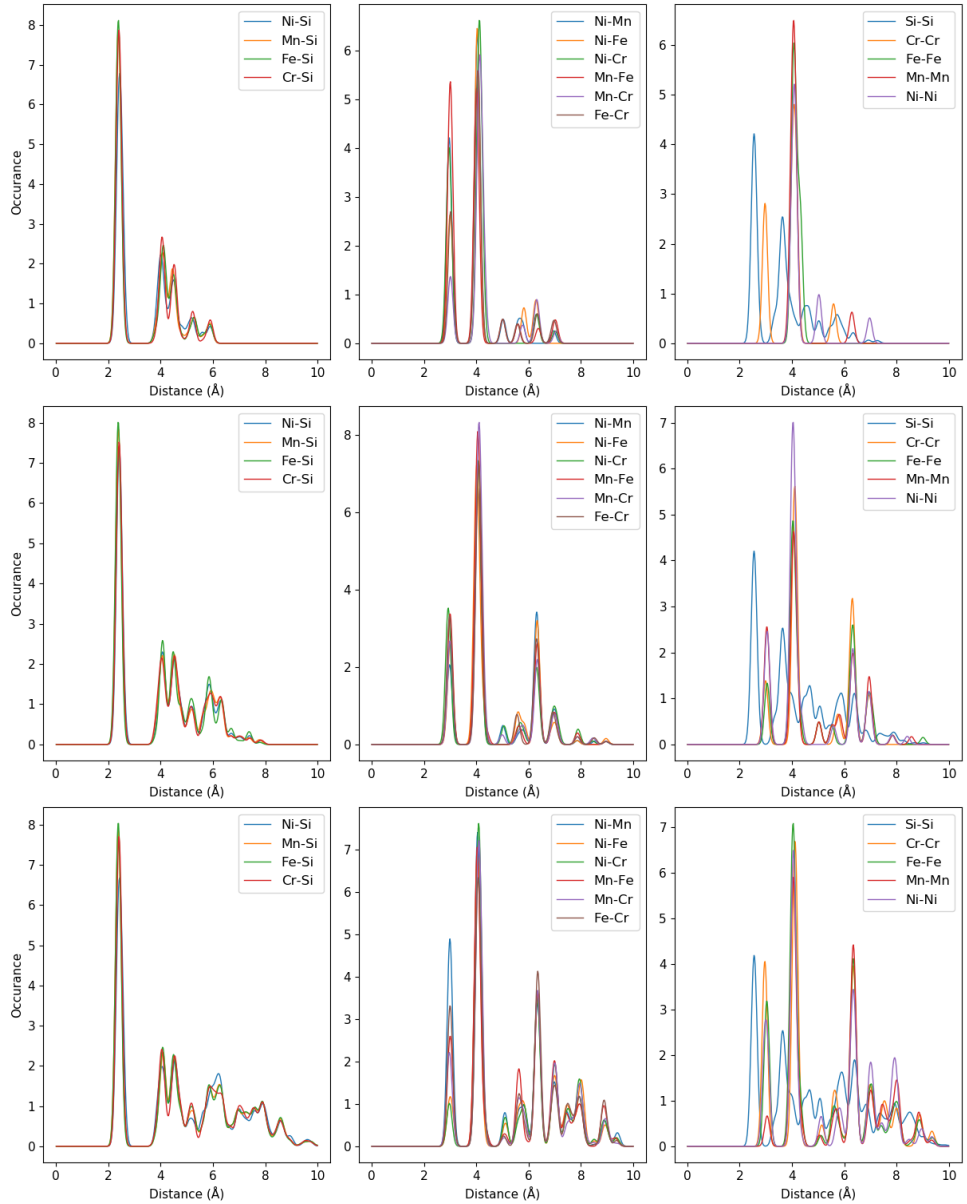


Figure 7.14: Pair distribution functions of $(\text{CrFeMnNi})\text{Si}_2$ (top) 48-atom SQS, (middle) 96-atom SQS, (bottom) 192-atom SQS.

Chapter 8

Alternative compositions

Up until this point we have looked in detail at the high-entropy silicide $(\text{CrFeMnNi})\text{Si}_2$. In this chapter we will broaden our search of compositions based on the $\beta - \text{FeSi}_2$ structure. First, we will look at various compositions inside the quaternary phase diagram of Cr, Fe, Mn and Ni, followed by compositions where chromium, manganese or nickel are replaced by cobalt or titanium.

8.1 Exploring the quaternary phase diagram

In this section, we aim to expand our search of this diagram by generating SQSs of the 48 atom model slightly away from equimolar distribution of 3d elements. The compositions we test are listed in table 8.1, with corresponding total energy, magnetic moment and formation energy in the familiar format. Ideally each composition would differ only by one element to provide a clear view of each direction in the phase diagram, but the TDEP implementation insist in reducing Nickel to stay consistent with the 48 atom supercell.

Composition	Toten (eV)		Mag (μ_B)		E_{FPA} (eV)
	mean	std	mean	std	
$\text{Cr}_3\text{Fe}_3\text{Mn}_7\text{Ni}_3\text{Si}_{32}$	- 6.6947	0.0040	0.1375	0.0186	-0.300
$\text{Cr}_5\text{Fe}_5\text{Mn}_3\text{Ni}_3\text{Si}_{32}$	- 6.6705	0.0030	0.1127	0.0223	-0.286
$\text{Cr}_5\text{Fe}_3\text{Mn}_5\text{Ni}_3\text{Si}_{32}$	- 6.6852	0.0041	0.1375	0.0456	-0.271
$\text{Cr}_3\text{Fe}_5\text{Mn}_5\text{Ni}_3\text{Si}_{32}$	- 6.6801	0.0036	0.0937	0.0209	-0.315
$\text{Cr}_3\text{Fe}_3\text{Mn}_3\text{Ni}_7\text{Si}_{32}$	- 6.3921	0.0078	0.0159	0.0101	-0.285

Table 8.1: Summary composition diagram

In table 8.1 we observe that moving away from the equimolar system result in both less and more stable alloys. Clearly the most lowest formation energies (most stable) correspond to compositions rich in manganese and poor in chromium. Likewise the least stable compositions in table

8.1 contain either increased amounts of Cr or reduced amounts of Mn compared to the equimolar system. In the equimolar composition the magnetic moment was attributed to primarily Cr and Mn atoms in the lattice. In table 8.1 we observe similarly that compositions rich in Cr and Mn exhibits the largest magnetic moments and vice versa. The band gaps of the respective compositions in five unique SQSs can be seen in table 8.2 below, calculated with PBE GGA.

Composition	SQS	$E_G^{\text{up, eigen}}(0.5)$ (eV)	$E_G^{\text{dw, eigen}}(0.5)$ (eV)	$E_G^{\text{tot, eigen}}(0.5, 0.5)$ (eV)
$\text{Cr}_3\text{Fe}_3\text{Mn}_7\text{Ni}_3\text{Si}_{32}$	A	0.3390	0	0
	B	0.4745	0	0
	C	0.1342	0	0
	D	0.1950	0.0063	0.0063
	E	0.4211	0	0
$\text{Cr}_5\text{Fe}_5\text{Mn}_3\text{Ni}_3\text{Si}_{32}$	A	0.003	0	0
	C	0.21	0	0
	D	0.0674	0.0413	0.0372
	E	0.362	0	0
$\text{Cr}_5\text{Fe}_3\text{Mn}_5\text{Ni}_3\text{Si}_{32}$	A	0.2082	0	0
	B	0.4053	0	0
	C	0.4659	0	0
	D	0.0843	0.0121	0.0121
	E	0.3008	0	0
$\text{Cr}_3\text{Fe}_5\text{Mn}_5\text{Ni}_3\text{Si}_{32}$	A	0.3922	0	0
	C	0.1285	0	0
	D	0.2595	0.1004	0.1004
	E	0.3591	0.1003	0.0848
$\text{Cr}_3\text{Fe}_3\text{Mn}_3\text{Ni}_7\text{Si}_{32}$	A	0	0	0
	B	0	0	0
	C	0	0	0
	D	0	0	0
	E	0.04	0	0

Table 8.2: Band gaps of various compositions of $(\text{CrFeMnNi})\text{Si}_2$. Most stable SQS of a set is highlighted in bold text, defect/impurity band gap are listed in cursive. Some SQSs were excluded from the table due to unsuccessful calculations.

From table 8.2 we observe that most compositions are half-metals alike the equimolar system with a spin up polarization. Each composition show large variation between configurations. We note $E_{G,\text{max}}^{\text{up}} \approx 0.5$ eV and $E_{G,\text{min}}^{\text{up}} \approx 0.1$ eV in both $\text{Cr}_3\text{Fe}_3\text{Mn}_7\text{Ni}_3\text{Si}_{32}$ and $\text{Cr}_5\text{Fe}_3\text{Mn}_5\text{Ni}_3\text{Si}_{32}$, and further $E_{G,\text{max}}^{\text{up}} \approx 0.4$ eV and $E_{G,\text{min}}^{\text{up}} \approx 0.1$ eV in $\text{Cr}_3\text{FeMn}_5\text{Ni}_3\text{Si}_{32}$. In all three of these compositions the proportion of manganese is increased relative

to the equimolar system, and two out of the three compositions contain reduced amounts of chromium. Looking at the two compositions with the least indication of a band gap $\text{Cr}_5\text{Fe}_5\text{Mn}_3\text{Ni}_3\text{Si}_{32}$ and $\text{Cr}_3\text{Fe}_3\text{Mn}_3\text{Ni}_7$, these contain reduced amounts of manganese. Thus, based on the few compositions tested in this experiment we can state a relation of the band gap mainly to manganese, but also chromium.

Based on the utmost stable configuration of each composition, we observe very encouraging results in the $\text{Cr}_3\text{Fe}_3\text{Mn}_7\text{Ni}_3\text{Si}_{32}$ composition with the largest E_G^{up} of the set of configurations, likewise the most stable SQS of the $\text{Cr}_5\text{Fe}_5\text{Mn}_3\text{Ni}_3\text{Si}_{32}$ composition is a semiconductor with a total band gap of about 0.1 eV. In the composition $\text{Cr}_5\text{Fe}_5\text{Mn}_3\text{Ni}_3\text{Si}_{32}$ the most stable SQS predicts a defect or impurity band gap as we discussed previously where the eigenvalues return a finite band gap despite of defect states. However we have not been able to investigate the nature and effect of this impurity band gap to further extent, likewise for the similar impurity gaps listed in table 8.2 and the 0 band gaps in spin down. Below in figures 8.1 and 8.2 we include the projected density of states around E_F of the utmost stable SQS of each composition. Because we only include and discuss the most stable SQS, the features of these figures can be subject to the uniqueness of that particular SQS rather than a distinct feature of the exact composition, but as stated previously the most stable configuration provide the most likely properties of the composition within the scope of this project.

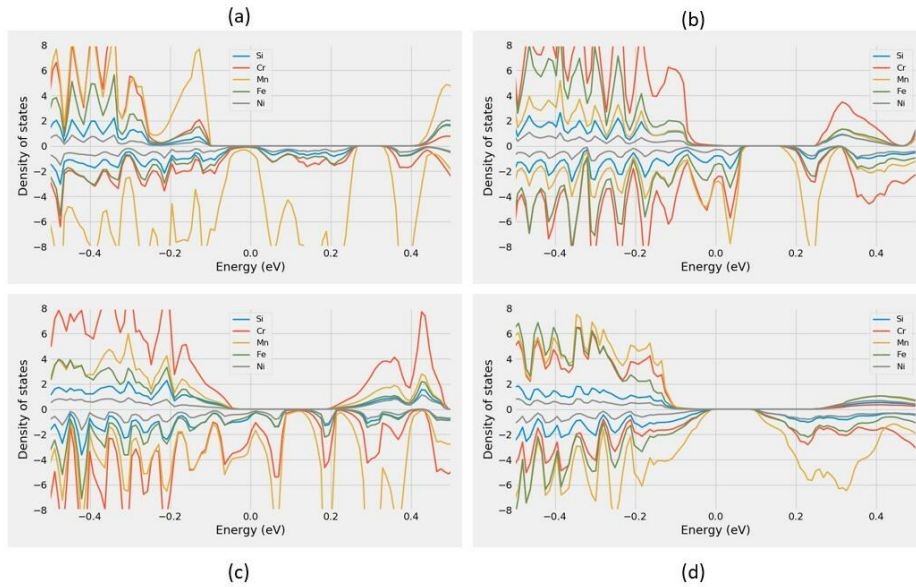


Figure 8.1: Projected density of states of (a) $\text{Cr}_3\text{Fe}_3\text{Mn}_7\text{Ni}_3\text{Si}_{32}$ (SQS B), (b) $\text{Cr}_5\text{Fe}_5\text{Mn}_3\text{Ni}_3\text{Si}_{32}$ (SQS C), (c) $\text{Cr}_5\text{Fe}_3\text{Mn}_5\text{Ni}_3\text{Si}_{32}$ (SQS A), (d) $\text{Cr}_3\text{Fe}_5\text{Mn}_5\text{Ni}_3\text{Si}_{32}$ (SQS D)

The PDOs is in good agreement with the listed values in table 7.2. $\text{Cr}_3\text{Fe}_3\text{Mn}_7\text{Ni}_3\text{Si}_{32}$ and $\text{Cr}_5\text{Fe}_3\text{Mn}_5\text{Ni}_3\text{Si}_{32}$ both display sizable band gaps in

spin, while figure 8.1 d point to a total band gap around 0.1 eV for SQS D of $\text{Cr}_3\text{Fe}_5\text{Mn}_5\text{Ni}_3\text{Si}_{32}$. On the other hand we observe as for the 192-atom SQS a dissimilarity between the density of states band gap in $\text{Cr}_5\text{Fe}_5\text{Mn}_3\text{Ni}_3\text{Si}_{32}$ SQS C (figure 8.1 b) and the eigenvalue (impurity) band gap listed in table 7.2. This can be better understood by figure .. in appendix .. that display a zoomed in DOS that clearly show small finite values at E_F in spin up. This DOS may resemble that of a n-doped material where the Fermi energy is pushed up in energy.

In figure 7.7 we saw that manganese distinctly occupied states in the spin down channel around E_F and was a key contributor as to why the spin down channel of $(\text{CrFeMnNi})\text{Si}_2$ was metallic in the utmost stable SQS. This is also largely the case in the compositions shown above in figure 8.1 and 8.2, and is particularly evident in figure 8.1 where Mn dominate the spin down states around E_F in the $\text{Cr}_3\text{Fe}_3\text{Mn}_7\text{Ni}_3\text{Si}_{32}$ composition. By reducing the number of Mn we still find that the Mn states prohibit the band gap in spin down, as seen in figure 8.1 b. In the chromium rich compositions plotted in figures 8.1 b and c, we observe that also Cr states prohibit the spin down band gap, and dominate states near E_F in spin up as well. Contrary, in the $\text{Cr}_3\text{Fe}_3\text{Mn}_3\text{Ni}_7\text{Si}_{32}$ composition plotted in figure 8.2, we do not observe any distinct peaks of elements, but rather consistent small finite DOS around E_F in all elements. The sole composition with clear evidence of a spin down gap is from the chromium poor system plotted in figure 8.1 d. Also in this structure we see that the effects of Mn around E_F is dominant in spin down from the relative large amounts of Mn, but in comparison to the other composition these states are pushed away from the Fermi energy.

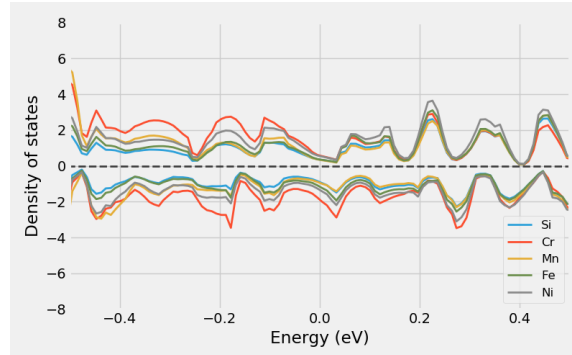


Figure 8.2: Projected density of states of $\text{Cr}_3\text{Fe}_3\text{Mn}_3\text{Ni}_7\text{Si}_{32}$ around E_F

An important factor of these results is that because each composition alters simultaneous elements, interpreting and relating the results to a particular alteration is challenging. For example, is the result of the $\text{Cr}_5\text{Fe}_3\text{Mn}_5\text{Ni}_3\text{Si}_{32}$ permutation a consequence of less Fe or increments to both Cr and Mn? Furthermore is the large band gap in spin up of $\text{Cr}_3\text{Fe}_3\text{Mn}_7\text{Ni}_3\text{Si}_{32}$ a product of increasing manganese or reducing the other elements. From the comparatively large gaps in spin up of $\text{Cr}_3\text{Fe}_3\text{Mn}_7\text{Ni}_3\text{Si}_{32}$ and $\text{Cr}_3\text{Fe}_5\text{Mn}_5\text{Ni}_3\text{Si}_{32}$ and the more present Cr states in spin up in the Cr rich permutations we here conclude that the band gap

is related to lessening of chromium, more so than other effects. However we see from both $\text{Cr}_5\text{Fe}_5\text{Mn}_4\text{Ni}_3\text{Si}_{32}$ and $\text{Cr}_3\text{Fe}_3\text{Mn}_3\text{Ni}_7\text{Si}_{32}$ (figure 8.2) in addition to the manganese rich composition that Mn plays a vital role on the band gap of these structures. It's clear that the $\text{Cr}_3\text{Fe}_5\text{Mn}_5\text{Ni}_3\text{Si}_{32}$ alloy manage to strike a balance between 3d elements that results in a specific interplay and correspondingly very promising properties. It would have been beneficiary to look at for example the pair distribution functions and compare to the equimolar system, but from the factors discussed in section 7.2.4 we leave this to future work.

As stated before, we relied on the PBE GGA functional to determine the band gap in this part from its reliability and favorably computation cost. However we have conducted calculations with SCAN and HSE06 on some of the more promising structures. For instance in SQS D of $\text{Cr}_3\text{Fe}_5\text{Mn}_5\text{Ni}_3\text{Si}_{32}$ we get lower values in both spin up and down with SCAN, specifically $E_{G,\text{SCAN}}^{\text{up}} = 0.21 \text{ eV}$ and $E_{G,\text{SCAN}}^{\text{dw}} = 0.08 \text{ eV}$, and on the other hand HSE06 predicts $E_{G,\text{HSE06}}^{\text{up}} = 0.53 \text{ eV}$ and $E_{G,\text{HSE06}}^{\text{dw}} = 0 \text{ eV}$. In SQS B of $\text{Cr}_3\text{Fe}_3\text{Mn}_7\text{Ni}_3\text{Si}_{32}$ we observe very different outcomes. With SCAN we get a small band gap in spin down of about 0.002 eV and 0 in spin up, likewise the HSE06 band gap of this structure is $E_{G,\text{HSE06}}^{\text{up}} = 0.08 \text{ eV}$ and $E_{G,\text{HSE06}}^{\text{dw}} = 0.11 \text{ eV}$, opposed to $E_{G,\text{PBE}}^{\text{up}} = 0.47 \text{ eV}$ and $E_{G,\text{PBE}}^{\text{dw}} = 0 \text{ eV}$. Further the HSE06 band gap is in fact an impurity band gap, with $E_{G,\text{HSE06}}^{\text{up,eigen}}(0.01) = 0.18 \text{ eV}$ and $E_{G,\text{HSE06}}^{\text{dw,eigen}}(0.01) = 0.16 \text{ eV}$.

8.2 High entropy silicides with cobalt/titanium

In similar fashion to the preceding section, we begin by presenting the new high-entropy silicides by the mean and standard deviation of the total energy and magnetization of 5 unique SQSs of each alloy in table 8.3. The compositions we have tested are deliberate combinations intended to investigate the role elements in the $(\text{CrFeMnNi})\text{Si}_2$ system, by introducing Co/Ti at the cost of different elements. Note that the alloys contain a total of 48 atoms as before, based on the $\beta - \text{FeSi}_2$ unit cell and equimolar distribution of 3d elements.

Composition	Toten (eV)		Mag (μ_B)		E_{FPA} (eV)
	mean	std	mean	std	
$\text{Cr}_4\text{Fe}_4\text{Co}_4\text{Ni}_4\text{Si}_{32}$	-6.4655	0.0056	0.0083	0.0155	-0.308
$\text{Co}_4\text{Fe}_4\text{Mn}_4\text{Ni}_4\text{Si}_{32}$	-6.4731	0.0046	0.0000	0.0000	-0.355
$\text{Cr}_4\text{Fe}_4\text{Ti}_4\text{Ni}_4\text{Si}_{32}$	-6.4217	0.0087	0.0305	0.0293	-0.209
$\text{Cr}_4\text{Fe}_4\text{Mn}_4\text{Ti}_4\text{Si}_{32}$	-6.6994	0.0071	0.1142	0.0641	-0.199
$\text{Cr}_4\text{Fe}_4\text{Mn}_4\text{Co}_4\text{Si}_{32}$	-6.7687	0.0034	0.1331	0.0326	-0.323

Table 8.3: Overview new compositions

In terms of the formation energy, we observe that cobalt evidently yield

the utmost stable alloys from the tested compositions, with $(\text{CoFeMnNi})\text{Si}_2$ at the top and $(\text{CrFeCoNi})\text{Si}_2$ at the bottom. On the other side, both $(\text{CrFeTiNi})\text{Si}_2$ and $(\text{CrFeMnTi})\text{Si}_2$ where we introduce titanium in place of manganese and nickel respectively, result in the overall least stable compositions. A precise physical interpretation of the stability between compositions is challenging from the shallow analysis in this project, but we do note that the two most stable alloys consist of the most chemically similar elements with respect to properties such as the electronegativity and atomic size. Following the least stable alloys are comprised of the most chemically dissimilar elements. This is in good agreement with the discussion in section 2.2 regarding phase formation of high-entropy alloys. Additionally, in the compositions discussed in the previous section we found that the most stable composition was $\text{Cr}_3\text{Fe}_5\text{Mn}_5\text{Ni}_3\text{Si}_{32}$ where the Cr proportion was lessened. In conjunction with the results of the titanium we thus may suspect that smaller elements are ill-suited in this structure.

In line with the other compositions studied in this project, the magnetization is clearly related to chromium and manganese also in this case. This is seen by the overall lowest magnetic moments in the two compositions without these elements, and reversely the highest magnetic moments is found for compositions with both Cr and Mn. Comparing the magnetic moment of $(\text{CrFeCoNi})\text{Si}_2$ and $(\text{CoFeMnNi})\text{Si}_2$ it seems in our study that chromium is most responsible for the magnetic moment in these alloys. Furthermore we find that substituting Ni with both Ti and Co yields more magnetic compounds. As we have discussed previously, the uniqueness of each SQS makes it difficult to draw conclusion on the various properties. In table 8.4 below we list the magnetic moment of the utmost stable SQS in each alloy. Contrary to the mean value we find that $(\text{CrFeCoNi})\text{Si}_2$ equal to $(\text{CoFeMnNi})\text{Si}_2$ is nonmagnetic, moreover $(\text{CrFeMnTi})\text{Si}_2$ are less magnetic relative to both $(\text{CrFeMnCo})\text{Si}_2$ and $(\text{CrFeMnNi})\text{Si}_2$.

Composition	Magnetic moment (μ_B)
$\text{Cr}_4\text{Fe}_4\text{Co}_4\text{Ni}_4\text{Si}_{32}$	0
$\text{Co}_4\text{Fe}_4\text{Mn}_4\text{Ni}_4\text{Si}_{32}$	0
$\text{Cr}_4\text{Fe}_4\text{Ti}_4\text{Ni}_4\text{Si}_{32}$	0,0653
$\text{Cr}_4\text{Fe}_4\text{Mn}_4\text{Ti}_4\text{Si}_{32}$	0,0785
$\text{Cr}_4\text{Fe}_4\text{Mn}_4\text{Co}_4\text{Si}_{32}$	0,1666

Table 8.4: Final magnetic moment of the utmost stable SQS of each composition.

Thus, based on the utmost stable configurations we can state that replacing either Cr or Mn (with Co), removes the magnetic moment of the alloy. Furthermore we find that the magnetic moment is reduced when Ni is substituted with Ti, and increased by Co. However, while substituting manganese with Co yields a nonmagnetic alloy, Ti for Mn only slightly

reduces the magnetic moment.

In regards to the band gap, we find most to be metals. In table 8.5 we list the band gap of the utmost stable SQS of each composition, where the band gap is determined from the eigenvalues at different occupancy cutoff occ values to underline the effect of defect states. We find that increasing the criteria, in other words only consider states with occupancy above a certain threshold, the band gap become finite with $occ = 0.1$ and converge to around 0.02 – 0.06 eV depending on composition at $occ = 0.01$ and beyond.

Composition	occ	$E_G^{\text{up, eigen}}$ (eV)	$E_G^{\text{dw, eigen}}$ (eV)	$E_G^{\text{tot, eigen}}$ (eV)
CrFeCoNiSi_2	0.5	0	0	0
	0.1	0.00095	0.0399	0.00095
	0.01	0.063	0.063	0.063
CrFeTiNiSi_2	0.5	0.0067	0	0
	0.1	0.061	0.0087	0.0087
	0.01	0.061	0.037	0.037
CoFeMnNiSi_2	0.5	0	0	0
	0.1	0.0037	0.0037	0.0037
	0.01	0.0268	0.0268	0.0268
CrFeMnTiSi_2	0.5	0	0	0
	0.1	0.021	0.00049	0
	0.01	0.03	0.03	0.022
CrFeMnCoSi_2	0.5	0.461	0	0
	0.1	0.607	0.0218	0.0218
	0.01	0.607	0.0245	0.0245

Table 8.5: The band gap in spin up/down and total of the utmost stable SQS in five high-entropy silicides based on $\beta\text{-FeSi}_2$

The CrFeMnCoSi_2 composition exhibits a band gap of around 0.5 eV in spin up, contrary to the metallic compositions. We observe that the gap similar to the $\text{Cr}_5\text{Fe}_5\text{Mn}_3\text{Ni}_3\text{Si}_{32}$ composition and the the 192-atom SQS in section 7.2.5, is an impurity gap that contain a small number of defect states in addition to the finite gap. As was the case in these structures, the band gap in $(\text{CrFeMnCo})\text{Si}_2$ display small nonzero DOS at the Fermi energy, as seen from the projected density of states in figure 8.3. As observed in the previous compositions, the PDOS in this alloy point to a severe number of manganese states in spin down at energies just above E_F , and further large number of Cr states right below E_F in spin up.

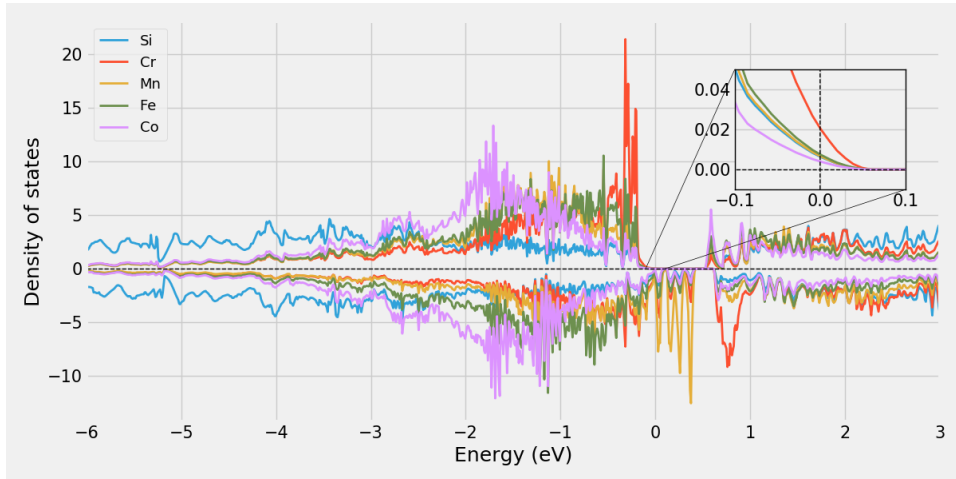


Figure 8.3: Projected density of states of $(\text{CrFeMnCo})\text{Si}_2$.

The PDOS of the other four alloys are included in figure 8.4 below. In agreement with the values listed in table 8.5 we observe clear indication of metallic structures, furthermore in agreement with the magnetic moments discussed previously.

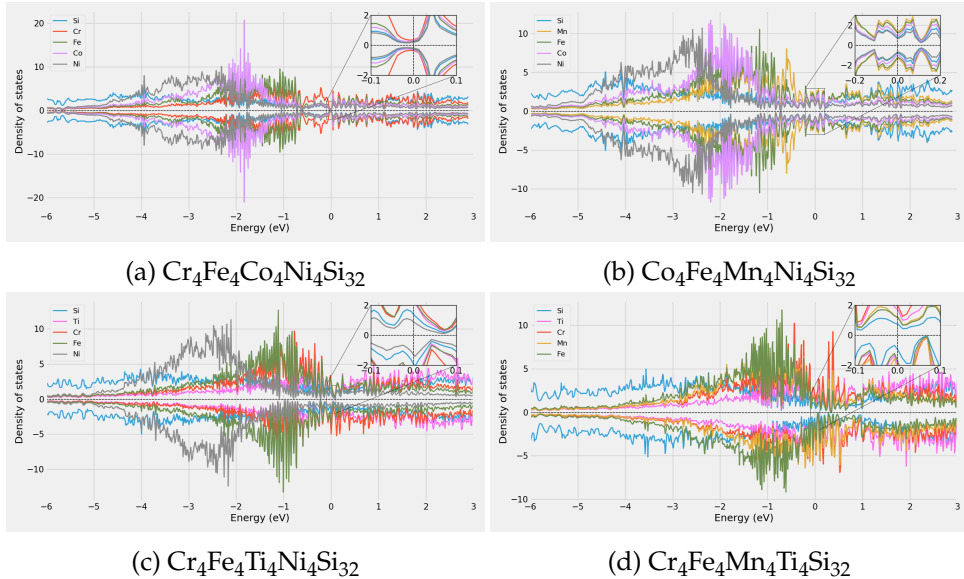


Figure 8.4: Projected density of states

Above we have evaluated the band gap of the different alloys based on the most stable configuration. Across all five configurations we find that the band gap is more or less consistent in $(\text{CrFeCoNi})\text{Si}_2$, (CrFeMnTiSi_2) , $(\text{CrFeTiNi})\text{Si}_2$ and $(\text{CrFeMnCo})\text{Si}_2$. The most interesting case is the CoFeMnNiSi_2 alloy, where we observed very narrow total band gaps in two lesser stable configurations (SQS A and E) of 0.03 eV and 0.006 eV respectively. Opposite of the impurity gaps discussed above, these are apparent in the density of states plots, as seen in figure 8.5 below.

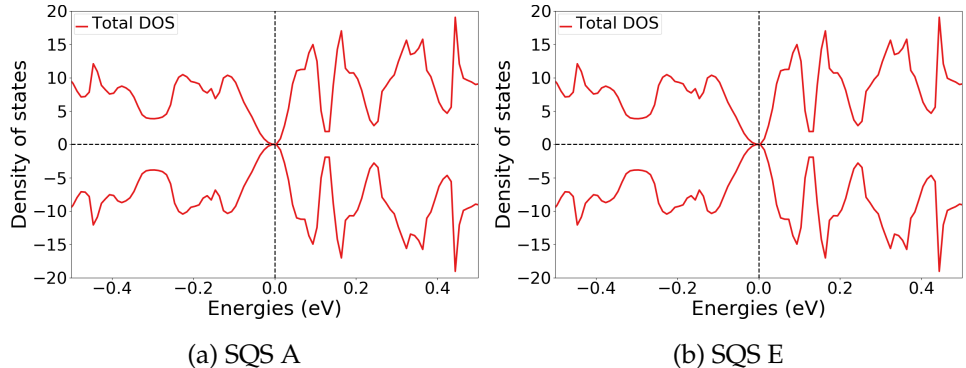


Figure 8.5: Density of states of two SQS A and E of $(\text{CoFeMnNi})\text{Si}_2$.

Besides the two structures above that exhibits small total band gaps in the meV range, in addition to the impurity gap in $(\text{CrFeMnCo})\text{Si}_2$ composition, we experience very limited success in our search for semiconducting high-entropy silicides compared to particularly the equimolar $(\text{CrFeMnNi})\text{Si}_2$ system. Alongside the equimolar composition where we observed moderate E_G^{up} of 0.3 eV and total band gaps close to 0.05 eV with PBE in several configurations, additional promising alloys were located inside the quaternary phase-diagram of Cr, Fe, Mn and Ni. For example the $\text{Cr}_3\text{Fe}_5\text{Mn}_5\text{Ni}_3\text{Si}_{32}$ composition with a total band gap of 0.1 eV, or $\text{Cr}_3\text{Fe}_3\text{Mn}_7\text{Ni}_3\text{Si}_{32}$ and $\text{Cr}_5\text{Fe}_3\text{Mn}_5\text{Ni}_3\text{Si}_{32}$ with configurations resulting in $E_G^{\text{up}} \approx 0.5$ eV. It was attempted to replicate the CrFeMnNi system based on alternative silicides, such as hexagonal CrSi_2 , trigonal Fe_2Si , and tetragonal and orthorombic Mn_4Si_7 , but we found no indication of a band gap. Furthermore we have tested a few alloys consisting of Sc, V, Zn, and Cu as well, but found no band gaps in these compositions either. In this project we have not been able to thoroughly analyze each composition and qualitatively differentiate the semiconducting/half-metal compositions from the metals. However, clearly, the presence of impurity states in the band gap of random alloys impede and complicate the search for possible narrow gap high-entropy silicides. In this project we have found the defect states to be responsible for a metallic spin down channel especially, but also the spin up channel. By removing the defect states we find that most structures exhibits small band gaps in both channels. This would have been very instructive to analyze with the band structure, but due to the challenges posed by the SQS method this was not possible within the time frame of the project, equally a part by part analysis of the PDFs proved to demanding. Further we would have liked to study the band gap by more adapt methods. As SCAN in the majority of cases proved unreliable, and HSE06 to computational demanding. A byproduct of this is that there is a possibility that several compositions have been wrongly classified as metals by exclusive use of PBE GGA.

In addition to the variation between compositions, we have observed large deviation also between configurations of the same composition. Thus, in order to qualitatively affirm the band gap of these alloys we should have first and foremost tested multiple configurations of each

composition, and a larger number of SQS sizes to reduce variance and obtain a converged value of the band gap. Secondly, to decide on the most representative configuration we would have put special efforts into correctly/optimally specify the magnetic configuration of each SQS, and secondly study excited states of the alloys to account for entropic contributions to the stability that can become paramount to the stability through Gibbs energy at elevated temperatures. Possibly, the most promising compositions should be simulated by other methods such as MC/MD and CPA. Furthermore, we should test different crystal structures in addition to the orthorombic CMCE space group, as the local minima method of DFT does not guarantee that this is the most stable conformation. Nevertheless, based on the examples and efforts put into this project, we have found in particular one very promising high-entropy silicide with the composition $\text{Cr}_4\text{Fe}_4\text{Mn}_4\text{Ni}_4\text{Si}_{32}$ with a total band gap of around 0.05 eV and $E_G^{\text{up}} = 0.3$ eV. In respect to possible thermoelectric application, we stated in the introduction that based on recent findings of related thermoelectric properties and properties of HEAs, that if we could find a narrow band gap alloy this could become an efficient thermoelectric material. However, from the values we have calculated the band gap may be too small for a thermoelectric. On the other hand if we assume that the PBE functional underestimates the band gap by some 50%, there is a possibility of these materials becoming efficient thermoelectric materials. For example the HSE06 band of SQS B in the $(\text{CrFeMnNi})\text{Si}_2$ system of 0.18 eV is well suited for thermoelectric application. However future work on the specific thermoelectric properties such as high-temperature stability, Seebeck coefficient, electrical and thermal conductivity. A supplementary application of these alloys could be as spintronics, from the strong spin polarization of the band gap and overall sizable values in spin up.

Part IV

Conclusion

Write conclusion here

Appendix A

$\text{Cr}_4\text{Fe}_4\text{Mn}_4\text{Ni}_4\text{Si}_{32}$

A.1 Density of states

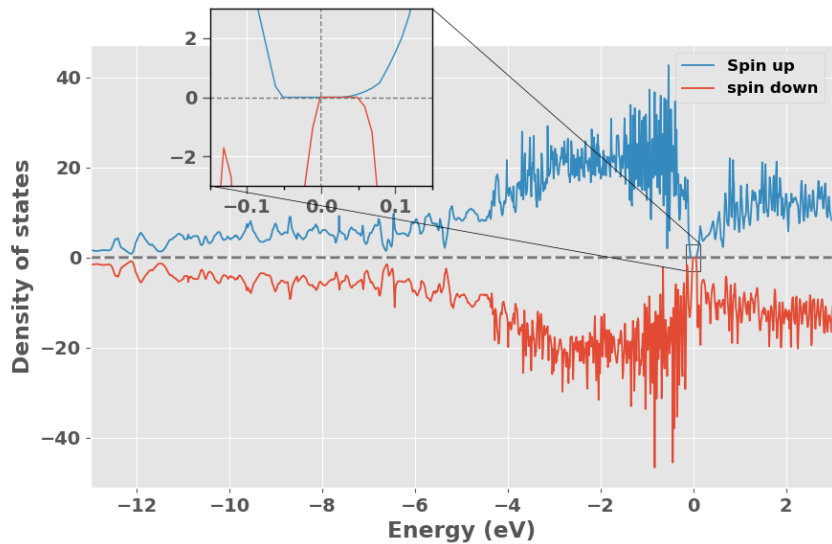


Figure A.1: Density of states SQS A ($\text{CrFeMnNi}\text{Si}_2$) with PBE.

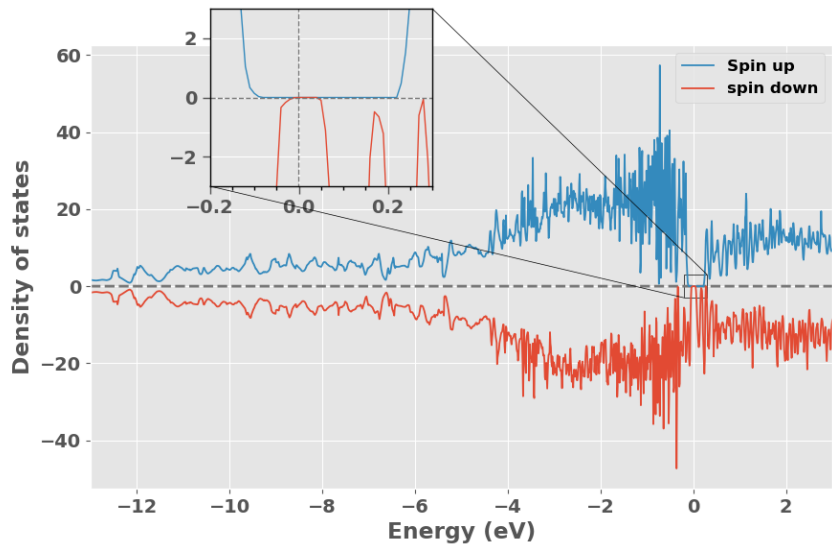


Figure A.2: Density of states SQS E (CrFeMnNi)Si₂ with PBE.

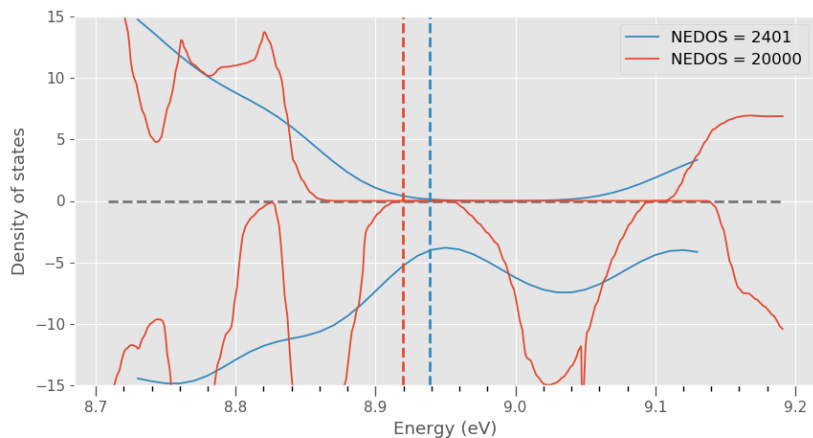


Figure A.3: Density of states SQS C (CrFeMnNi)Si₂ with PBE. Nedos represent the number of points in the DOS calculation.

A.2 Projected density of states

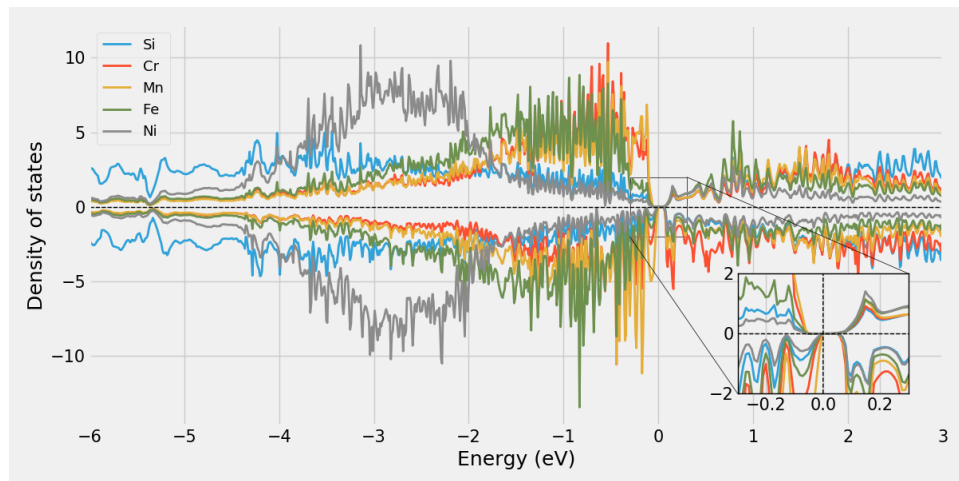


Figure A.4: Projected density of states SQS A

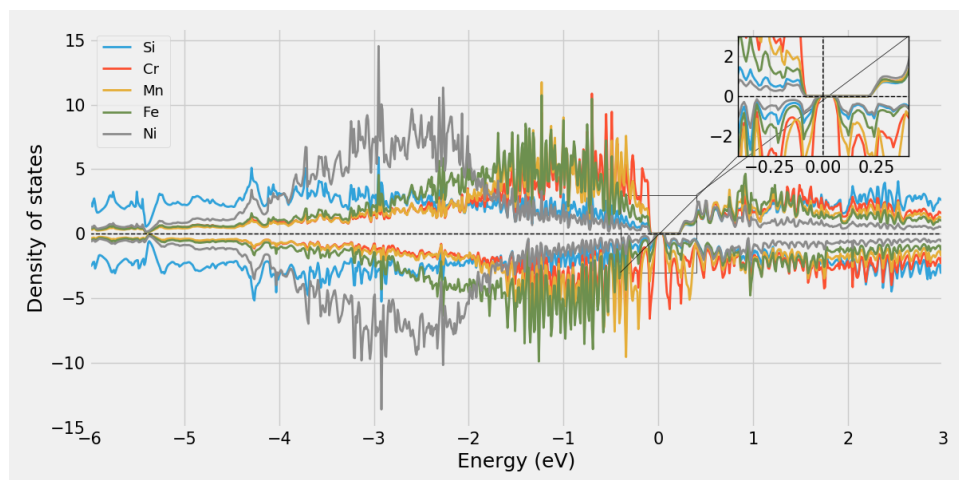


Figure A.5: Projected density of states SQS B

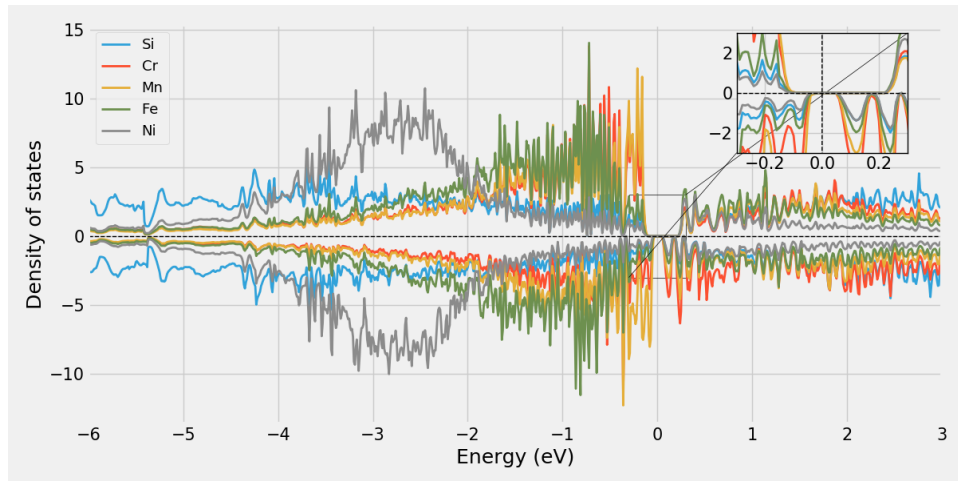


Figure A.6: Projected density of states SQS E

A.3 Charge density

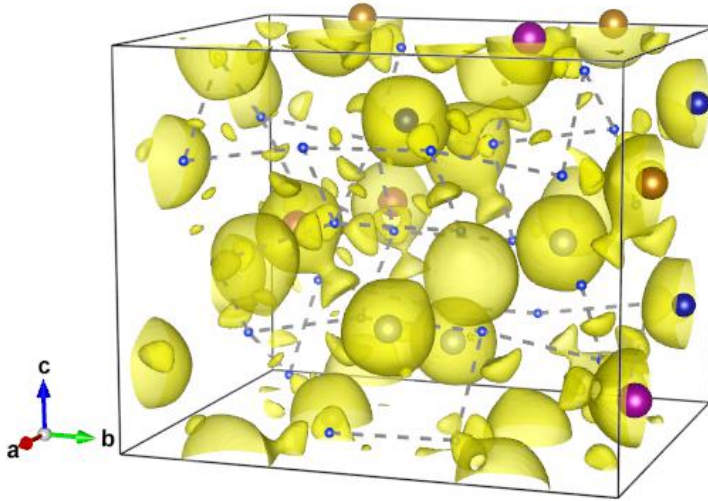


Figure A.7: Charge density of SQS C.

Appendix B

Alternative compositions

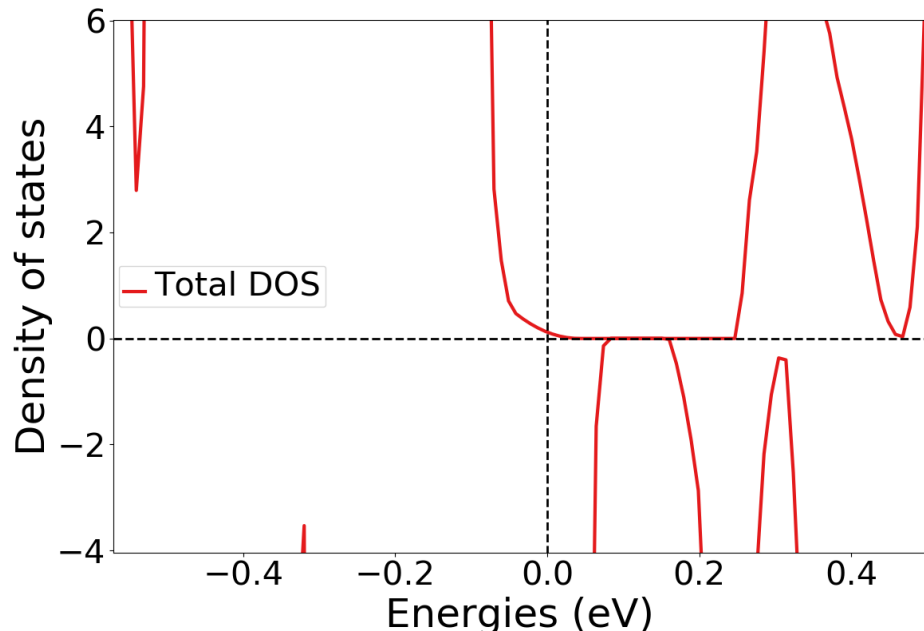


Figure B.1: Density of states SQS C $\text{Cr}_5\text{Fe}_5\text{Mn}_3\text{Ni}_3\text{Si}_{32}$, illustrating the small finite DOS at E_F due to the impurity gap.

Bibliography

- [1] S. J. Clark et al. ‘Structure and electronic properties of FeSi₂’. In: *Phys. Rev. B* 58 (16 Oct. 1998), pp. 10389–10393. DOI: 10.1103/PhysRevB.58.10389. URL: <https://link.aps.org/doi/10.1103/PhysRevB.58.10389>.
- [2] Voicu Popescu and Alex Zunger. ‘Effective Band Structure of Random Alloys’. In: *Phys. Rev. Lett.* 104 (23 June 2010), p. 236403. DOI: 10.1103/PhysRevLett.104.236403. URL: <https://link.aps.org/doi/10.1103/PhysRevLett.104.236403>.
- [3] H Lange. ‘Electronic properties of semiconducting silicides’. In: *physica status solidi (b)* 201.1 (1997), pp. 3–65.
- [4] R. Eppenga. ‘Ab initio band-structure calculation of the semiconductor β-FeSi₂’. In: *Journal of Applied Physics* 68.6 (1990), pp. 3027–3029. DOI: 10.1063/1.346415. eprint: <https://doi.org/10.1063/1.346415>. URL: <https://doi.org/10.1063/1.346415>.
- [5] ISMEAR - Vaspwiki. URL: <https://www.vasp.at/wiki/index.php/ISMEAR>.